Conductivity and structure of $M_{1-x}Pb_xF_2$ (M = Ca, Sr, Ba) solid solutions prepared by ball milling

Supporting Information

Andre Düvel

Institute of Physical Chemistry and Electrochemistry, Leibniz University Hannover, Hannover, Callinstr. 3-3a, 30167 Hannover, Germany.

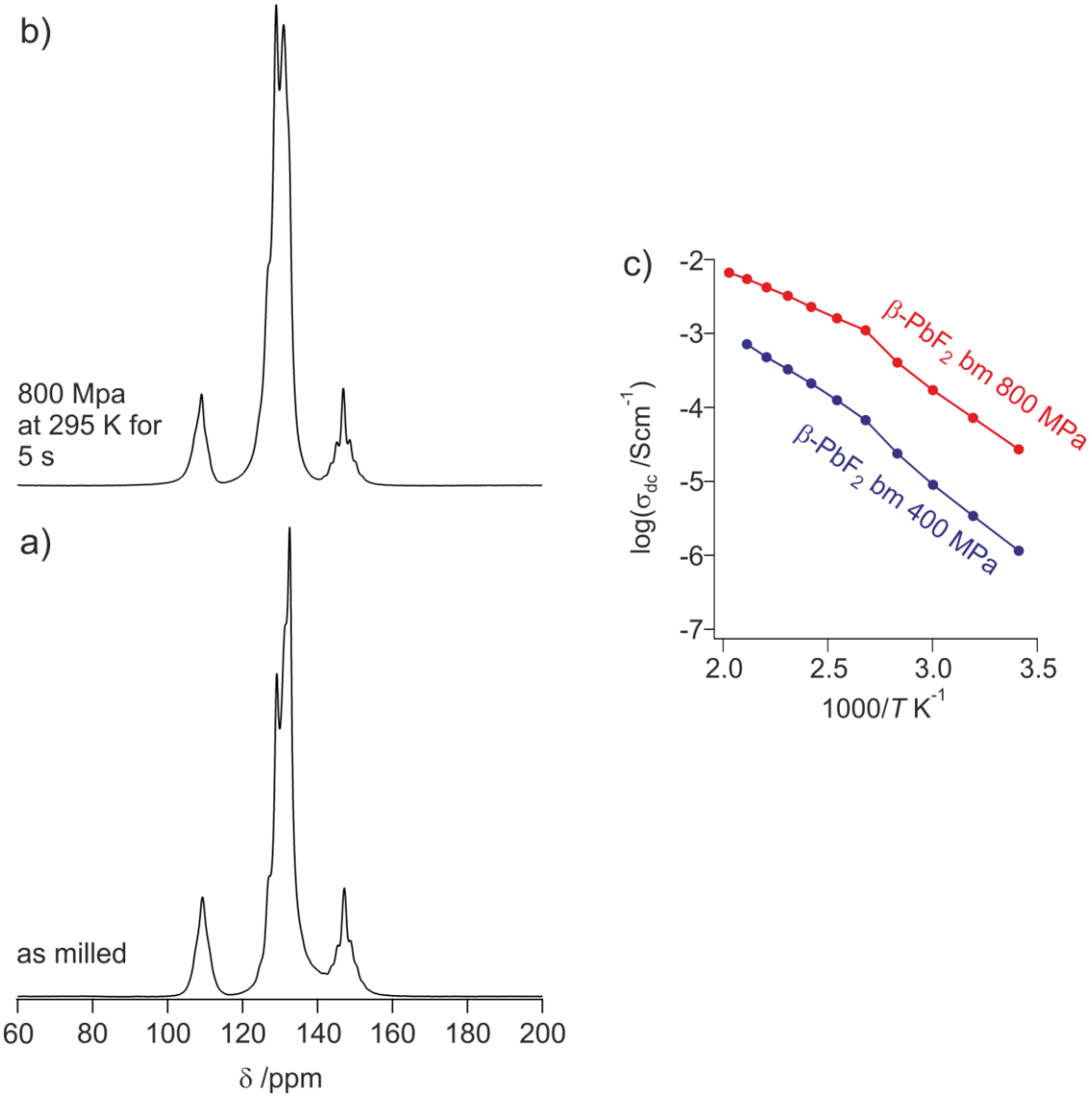

Fig. S1 ^{19}F MAS NMR spectra (ν_0 = 564.7 MHz, ν_{rot} = 60 kHz) of PbF_2 milled for 10 h, showing a large amount of β-PbF_2 before (a)) and after (b)) uniaxial pressing. The shape of the NMR line of the β-PbF_2 is probably affected by fluoride ion motion. c) Arrhenius plots of the conductivities of the sample pressed at two different pressures, showing a clearly lower dc conductivity of the pellet pressed at only 400 MPa, due to a lower density of the pellet.

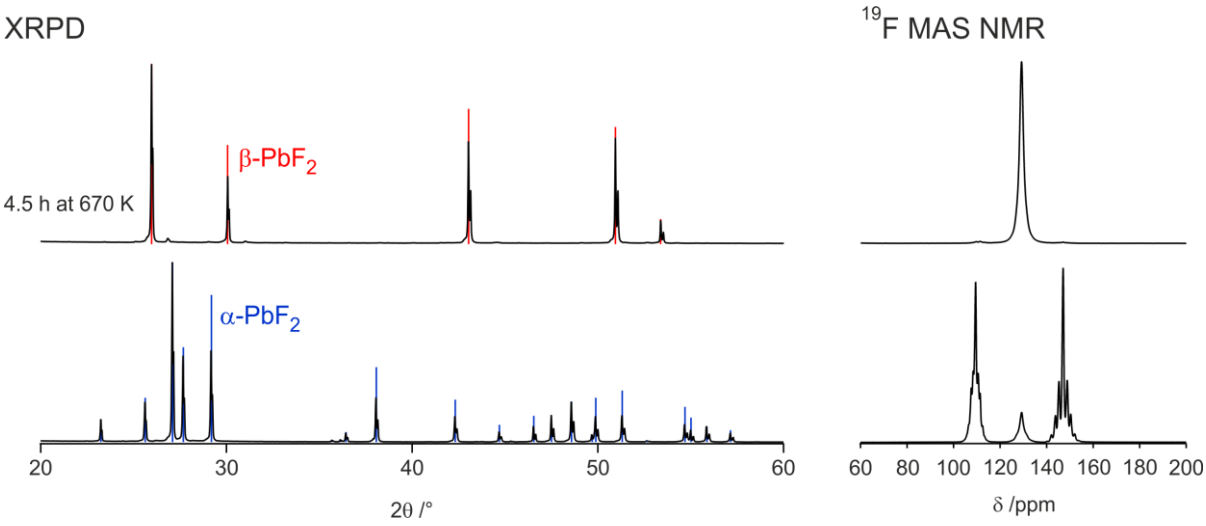

Fig. S2 XRPD pattern and ^{19}F MAS NMR spectra (ν_0 = 564.7 MHz, ν_{rot} = 60 kHz) of non-milled PbF_2 before and after annealing at 670 K in argon atmosphere. The NMR line of the fluorite-structured PbF_2 shows no splitting, which is probably due to fast fluoride ion motion, averaging out the ^{19}F-^{207}Pb coupling.

Since ^{19}F-^{207}Pb coupling is visible in the spectra of ball milled PbF_2 containing a large amount of β-PbF_2 (fig. S1), it seems that the fluoride ion mobility in the crystallites of the ball milled PbF_2 is smaller than in the crystallites of microcrystalline β-PbF_2.

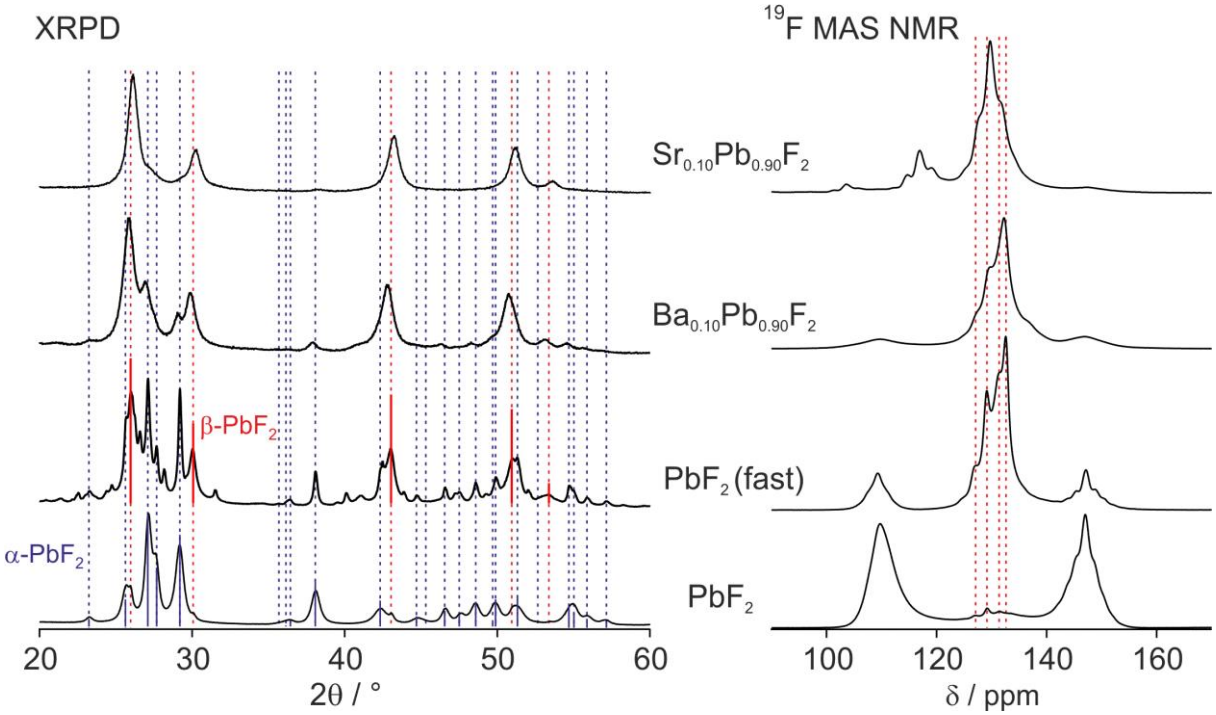

Fig. S3 XRPD patterns and ^{19}F MAS NMR spectra (ν_0 = 564.7 MHz, ν_{rot} = 60 kHz) of $Sr_{0.10}Pb_{0.90}F_2$, $Ba_{0.10}Pb_{0.90}F_2$ and two PbF_2 samples milled for 10 h, where one consists mainly of β-PbF_2, PbF_2 (fast), and the other mainly of α-PbF_2, PbF_2. The comparison with $Sr_{0.10}Pb_{0.90}F_2$ and $Ba_{0.10}Pb_{0.90}F_2$ shows clear differences to the ball milled PbF_2 with a large amount of β-PbF_2.

The XRPD pattern of the PbF_2 that exhibits a large amount of β-PbF_2 also shows several peaks that cannot be assigned to a known phase. No Pb_xF_y phase, $PbF_{x-2y}O_y$ or similar phases (oxides, carbonates, hydroxides, ...) can be fitted to the pattern. The ^{19}F MAS NMR shows only NMR lines of the orthorhombic and the cubic phase, which indicates that the unknown phase does not contain fluoride, or that its NMR lines are hidden by the NMR lines of the α- and β-PbF_2. Hence, the nature of the additional phase remains unknown.

Conductivity measurements

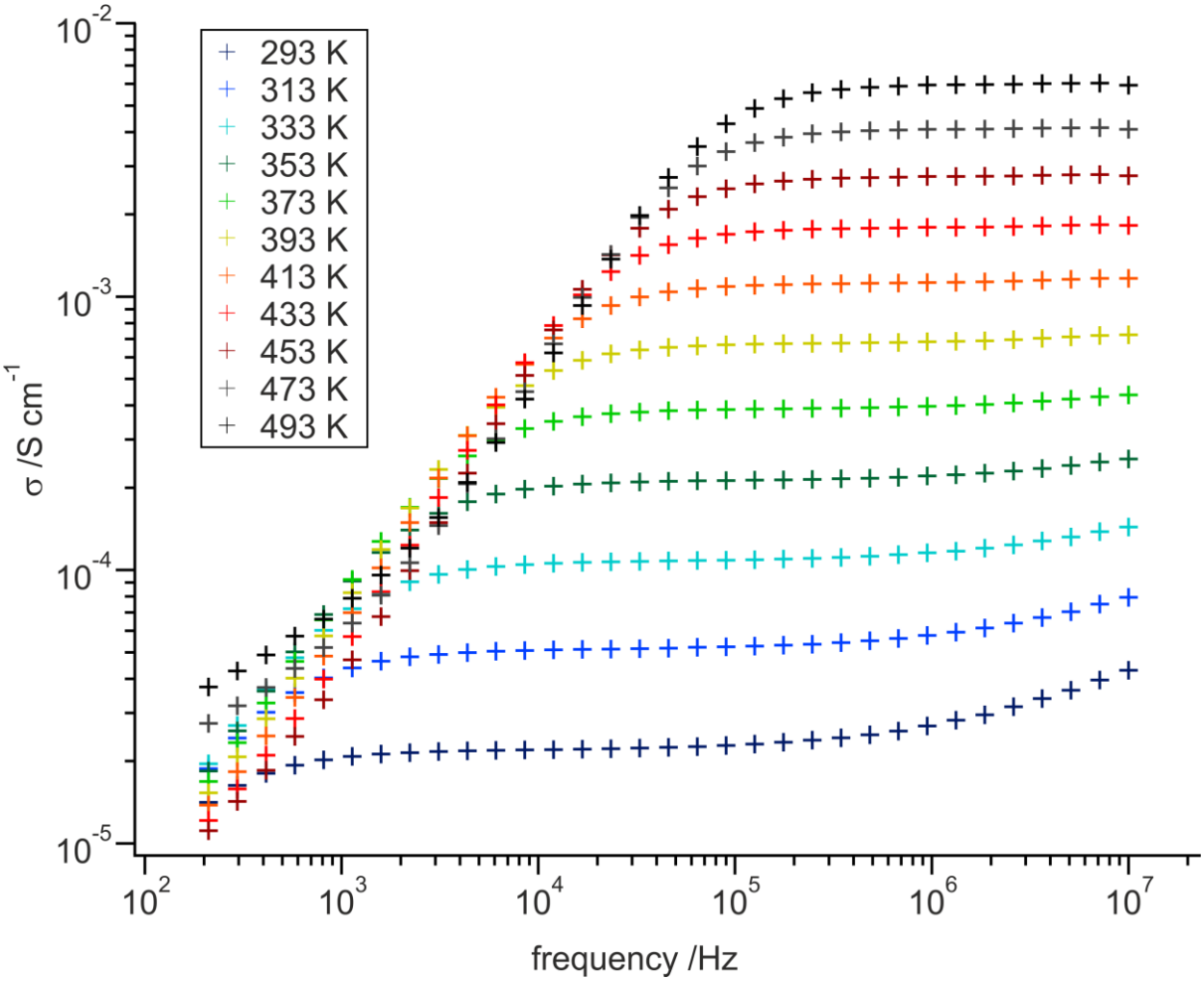

Fig. S4 Conductivity spectra of $Ca_{0.30}Pb_{0.70}F_2$ (milled for 10 h).

The conductivity spectra shown in fig. S3 are representative for the conductivity spectra of all other samples investigated within this study. The dc conductivity can be read out from the frequency independent plateaus. With decreasing frequency, the conductivity decreases, due to the ion blocking electrodes used for the measurements. With decreasing frequency an increasing part of the ions are stuck at the electrode, creating a decrease of the conductivity.

The frequency independent plateaus are shifting towards higher frequency with increasing temperature, due to the increasing velocity of the fluoride ions being able to follow the amplified electric field at increasingly high frequencies. Hence, the fluoride ions also have travelled to the ion blocking electrodes already at higher frequency, causing a decrease of the ionic conductivity at that frequency. If one would decrease the frequency towards 0 Hz, another plateau would emerge, exhibiting the electronic conductivity of the sample. Accordingly, the electronic conductivities of the samples are orders of magnitude

smaller than the ionic conductivity. At high frequencies, short ranged jump processes increase the conductivity further.

The activation energies of the conduction process can be calculated from Arrhenius plots of the conductivities, as shown exemplarily in fig. S5.

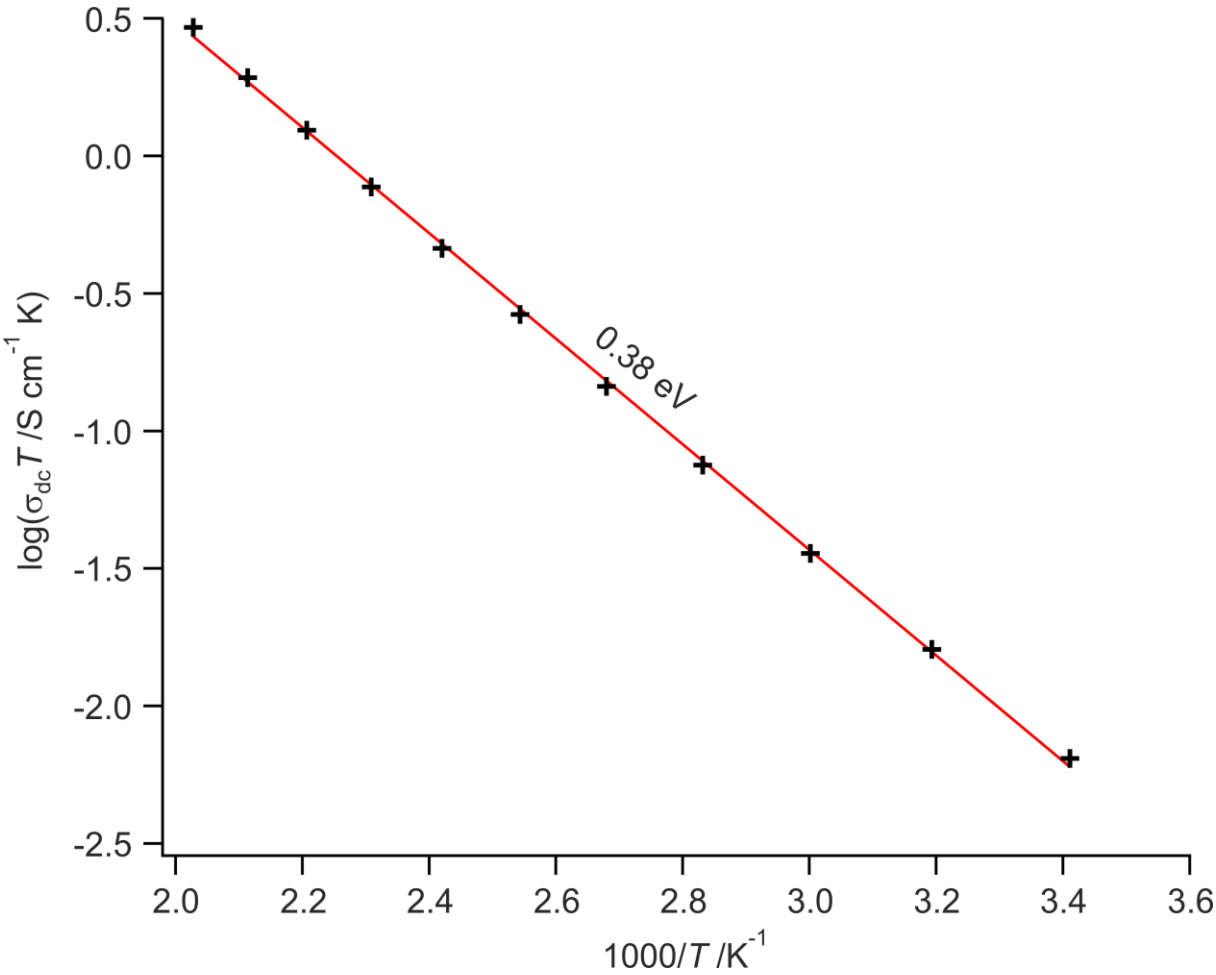

Fig. S5 Arrhenius plot of the conductivity of $Ca_{0.30}Pb_{0.70}F_2$ (milled for 10 h).

The activation energy, E_a, of the conduction process can be calculated with the following equation:

$\sigma_{dc}T = A \exp(-E_a/k_BT)$

T = temperature in K

k_B = Boltzmann's constant

A = pre-exponential factor

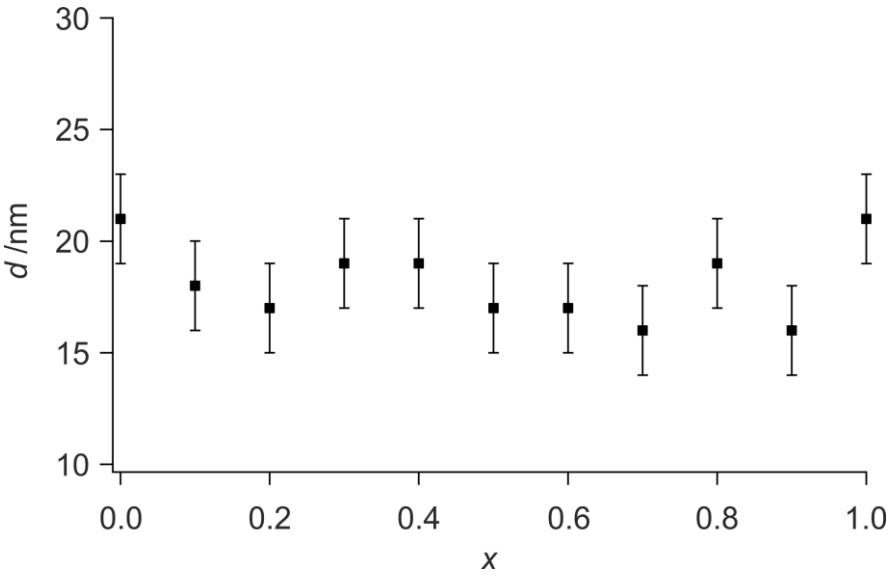

Fig. S6 Average crystallite sizes of $Sr_{1-x}Pb_xF_2$ estimated using Scherrer's equation, using a shape factor, *K*, of 0.9 assuming spherical crystallites.

Scherrer equation, with λ being the X-ray wave length (0.154 nm) and β the fwhm of the XRPD peaks reduced by 0.1° being the fwhm of a single crystalline material (instrumental broadening):

$$\langle d \rangle = \frac{K\lambda}{\beta \cos\theta}$$

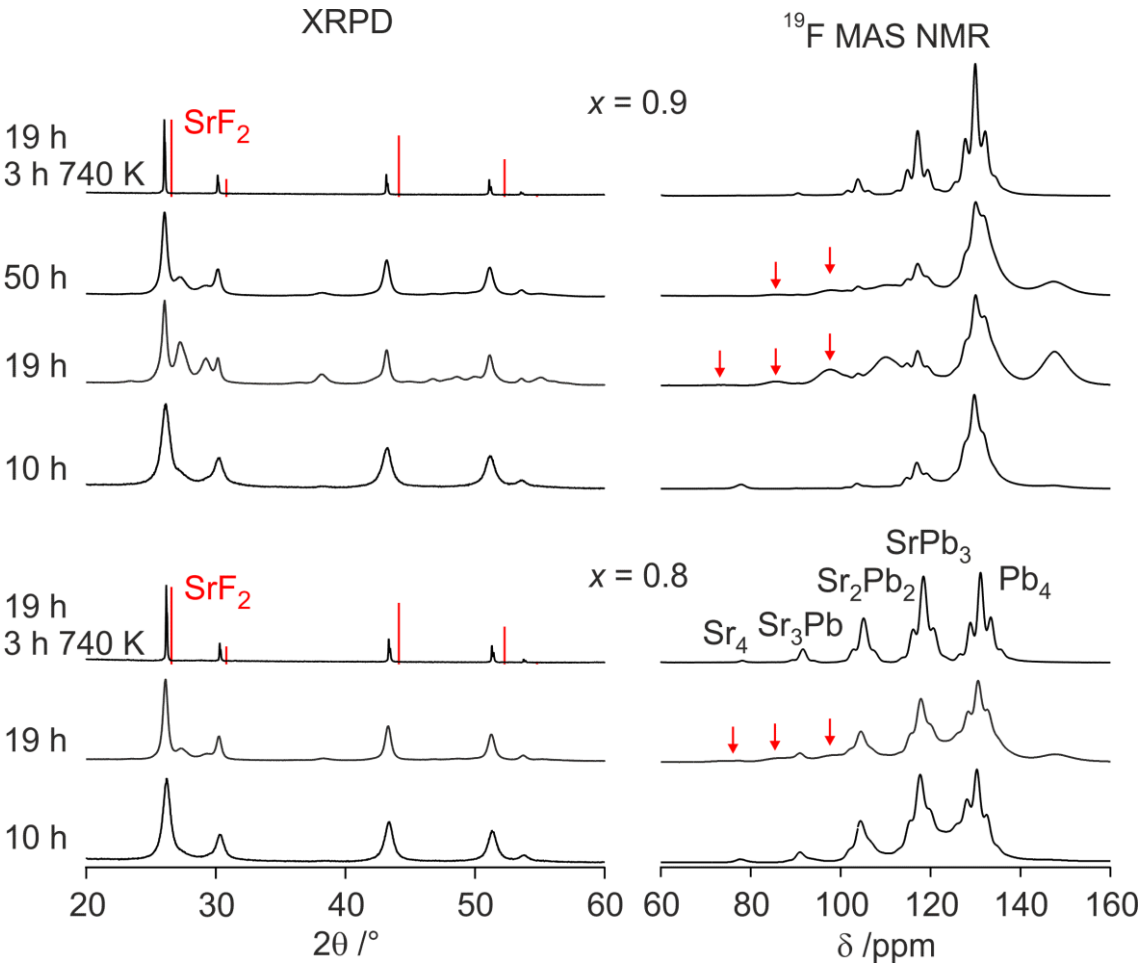

Fig. S7 XRPD patterns and ^{19}F MAS NMR spectra (ν_0 = 564.7 MHz, ν_{rot} = 60 kHz) of mixtures of SrF_2 and PbF_2, forming $Sr_{1-x}Pb_xF_2$, after two different milling times and after annealing the solid solutions. The arrows indicate additional NMR lines.

Origin of additional NMR lines in the ^{19}F MAS NMR spectra of $Sr_{0.20}Pb_{0.80}F_2$ and $Sr_{0.10}Pb_{0.90}F_2$ milled for 19 h and 50 h

The spacing of these NMR lines is similar to the spacing of the NMR lines that were assigned to the different fluoride ion environments in the fluorite-structured $Sr_{1-x}Pb_xF_2$, but it is slightly smaller. The chemical shifts themselves are smaller than the ones of the Sr_4, Sr_3Pb and Sr_2Pb_2 environments, respectively. Hence, these three lines might represent Sr_4, Sr_3Pb and Sr_2Pb_2 in $Sr_{1-x}Pb_xF_2$ but with larger distances between the fluoride ions and cations. Larger cation-fluoride distances are also in agreement with the smaller spacings between the NMR lines. Employing the superposition model introduced by Bureau et al.[1] (see also ref. 2) for fluorite-structured $Sr_{1-x}Pb_xF_2$ the chemical shifts can be reproduced by assuming a Sr-F distance of 0.2518 nm and a Pb-F distance of 0.2587 nm instead of 0.2512 nm and 0.257 nm in case of these environments in fluorite-structured $Sr_{0.30}Pb_{0.70}F_2$. Assuming a smaller Sr-F (Pb-F) distance leads to a larger Pb-F (Sr-F) distance to obtain the correct chemical shifts. This could mean, that longer milling favors the formation of a Sr-rich X-ray amorphous $Sr_{1-x}Pb_xF_2$ phase with an expanded lattice, instead of a Pb-rich $Sr_{1-x}Pb_xF_2$ next to a small amount of residual SrF_2. However, in amorphous material the interionic distances should decrease due to the lack of a Madelung field, see e.g. refs. 2,3. Thus, these expanded environments might be explained by assuming them being isolated in a PbF_2 matrix expanding the Sr-F distances, which

might be expected to be present in a Pb-rich $Sr_{1-x}Pb_xF_2$ solid solution like $Sr_{0.10}Pb_{0.90}F_2$. However, the Pb-F distance assumed to be present in these mixed environments is larger than in pure PbF_2. This could be explained by the fluoride ion being closer to the smaller Sr^{2+} than the Pb^{2+} ion, see fig. S8 for a sketch. Interestingly, these additional NMR lines cannot be found in the spectra of the samples that were prepared by ball milling for 19 h and then annealed for 3 h at 740 K (fig. S7). Expectedly, also the orthorhombic material vanishes after annealing. The intensities of the additional NMR lines correlate with the intensities of the NMR lines of fluoride on F1 and F2 sites of the orthorhombic $Sr_{1-x}Pb_xF_2$. Furthermore, the additional NMR lines have a similar shape as the ones of the F1 and F2 NMR lines, which are considerable broader than the ones of the fluorite-structured $Sr_{1-x}Pb_xF_2$. Hence, they might also represent mixed cation environments in cotunnite-structured $Sr_{1-x}Pb_xF_2$. A calculation of the chemical shifts of these environments with the superposition model[1] is not possible, since the ^{19}F chemical shifts of cotunnite-structured SrF_2 (forming at pressures of ca. 5 GPa[4]) are unknown. Furthermore, the different distances between the cations and fluoride ions in the cotunnite-structure leads to 12 different configurations in case of the F1 environment, of which all also will have altered cation-fluoride distances, due to the different ionic radii of Pb^{2+} and Ba^{2+}.

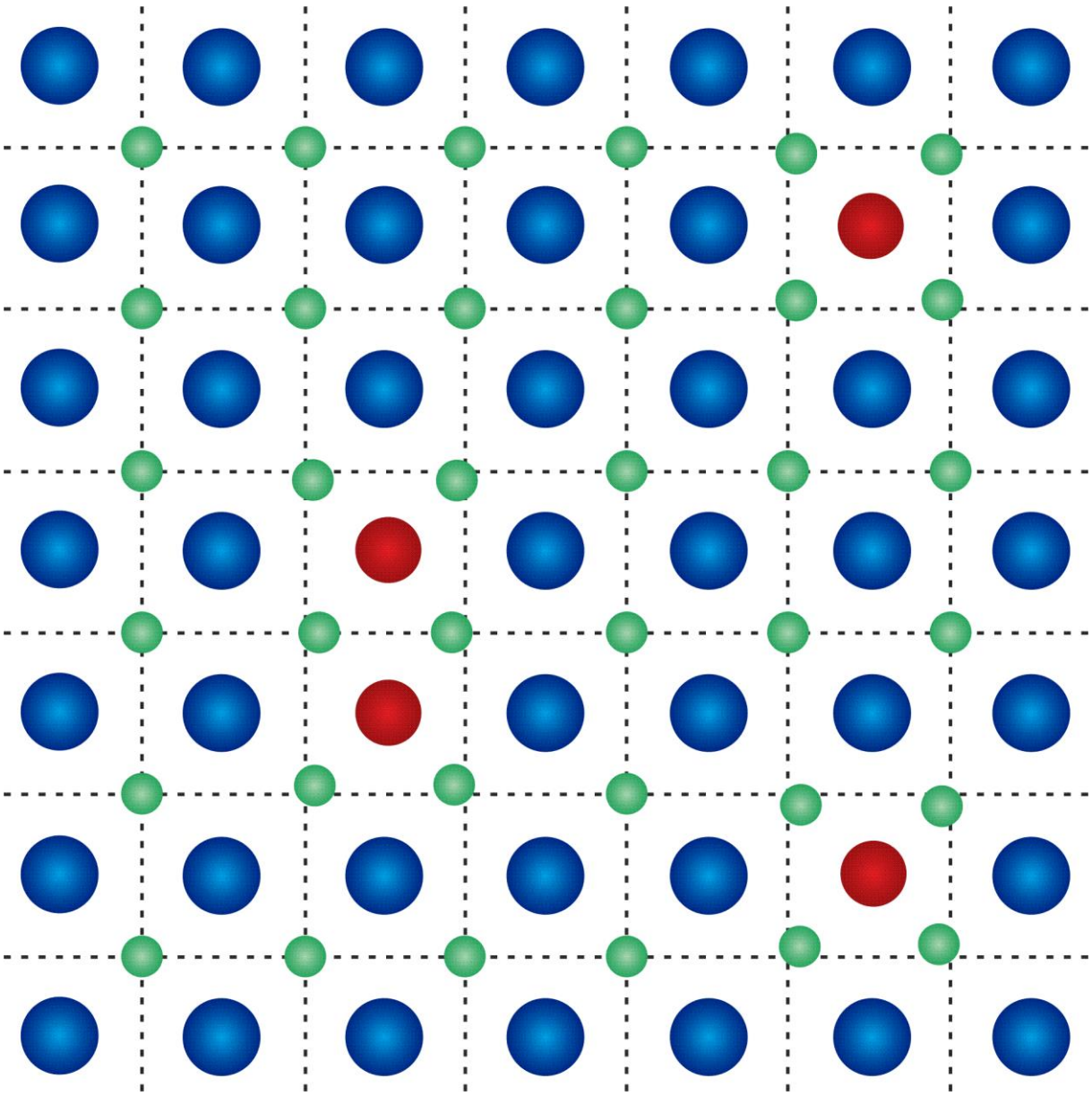

Fig. S8 Top view on fluorite structured PbF_2 doped with Sr^{2+}. Pb^{2+} is colored blue, Sr^{2+} is colored red, F^- is colored green. Fluoride ions are closer to Sr^{2+} than to Pb^{2+}, causing larger Sr-F and Pb-F distances than in pure SrF_2 and PbF_2.

The relative frequencies of the five cation environments can be calculated from the relative integrals of the NMR lines of the ^{19}F MAS NMR spectra. They can be compared with the relative frequencies expected in case of a random distribution of the two cation species, which can be calculated according to a binomial distribution:

$$I = \binom{n}{k} p^k q^{n-k}$$

with

$$\frac{n}{k} = \frac{n!}{k!\,(n-k)!}$$

I = relative frequency of respective cation environments $[FM^a_{4-x}M^b_x]$
$(0 \le x \le 4, x \in \mathbb{N})$

n = total number of cations in the first coordination sphere of the fluoride ion ($n = 4$)

k = number of positions occupied by Pb or alkaline earth metal (Ca, Sr, Ba)

p, q = relative ratio of the cation species ($q = 1\text{-}p$)

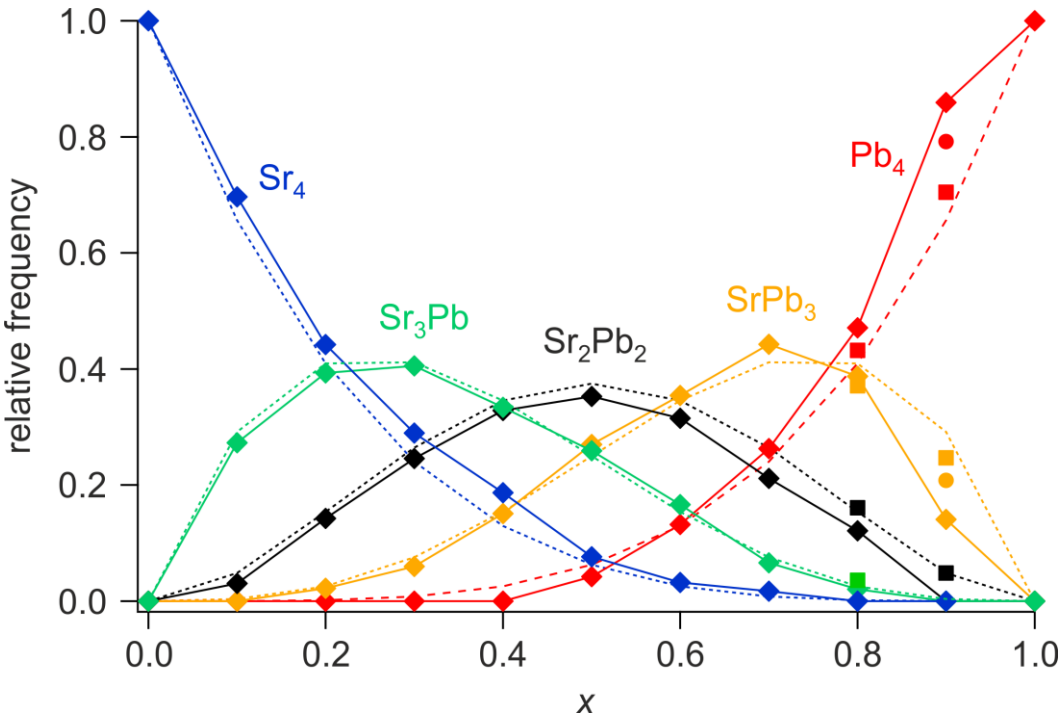

Fig. S9 Relative frequencies of the five cation environments of fluoride ions in $Sr_{1-x}Pb_xF_2$. The dotted lines show the relative frequencies of the environments in case of a random distribution of the two cation species. For x = 0.80 and x = 0.90 the values obtained after 19 h of milling are shown. The rectangles (x = 0.80 and x = 0.90) show the values obtained from the spectra of the annealed samples (see fig. S4), the circles show the values of $Sr_{0.10}Pb_{0.90}F_2$ prepared by milling for 50 h at 600 rpm.

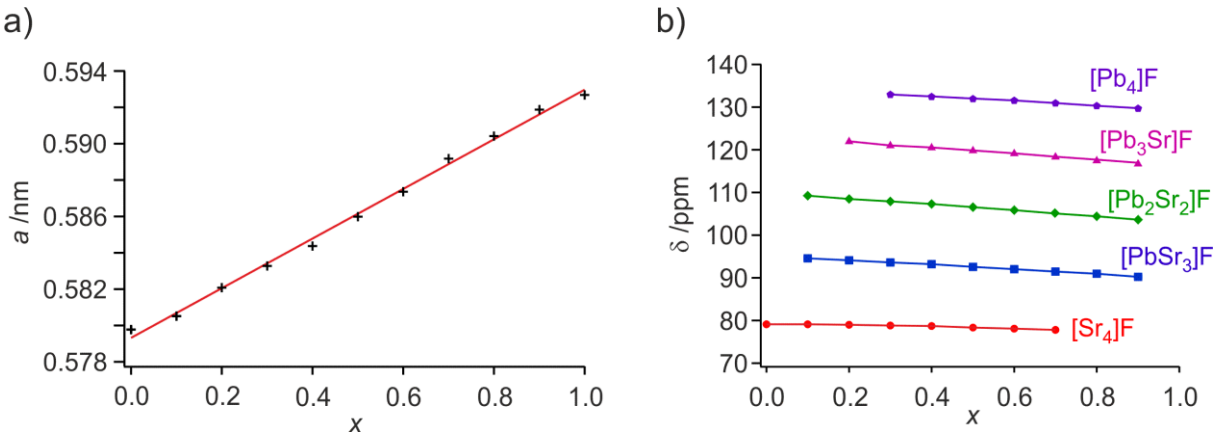

Fig. S10 a) Lattice parameter of $Sr_{1-x}Pb_xF_2$ as a function of x. b) Change of the ^{19}F chemical shifts of the five different environments of fluoride ions in fluorite-structured $Sr_{1-x}Pb_xF_2$ (the lines are meant to guide the eye).

Orthorhombic BaF_2

Orthorhombic BaF_2, a high-pressure polymorph of BaF_2 usually forms during ball milling BaF_2. Thus, it can be concluded that during ball milling pressures occur that are sufficient for the transformation to orthorhombic BaF_2.

The pressure of a milling ball hitting the wall can be estimated.

With milling balls made of stabilized ZrO_2 with a diameter of 5 mm, milling beakers with an inner diameter of ca. 4.7 cm, a rotational speed of 600 rounds per minute (rpm) and the largest distance between the milling beaker wall and the axis of the main disc of the planetary ball mill being 9.1 cm and a few rough assumptions we calculate:

The centrifugal acceleration a_{acc}:

$a_{acc} = v^2/r$

With v being the velocity of the milling ball and r its distance from the axis of the main disc.

With a rotational speed of 600 rpm, being 10 rounds per second,

$v = 20\pi r$

The initial velocity of the milling ball is unknown. Hence, we assume the starting velocity to be 0 m/s. For simplicity, as a starting point the smallest distance between the inner wall of the milling beaker and the axis of the main disc is used, giving the milling ball a distance of 4.65 cm for acceleration.

Acceleration happens from r_1 = 9.1 cm – 4.7 cm = 4.4 cm to r_2 = 9.1 cm – 0.025 cm = 9.075 cm.

$$a = \frac{(20\pi r)^2}{r}$$

$$\frac{\mathrm{d}a}{\mathrm{d}r} = 800\pi^2 r$$

$$\int_{r_1}^{r_2} 800\pi^2 r = 400\pi^2 (0.09075\ m)^2 - (0.044\ m)^2 \approx\ 24.87\ m/s^2$$

$$s = at^2 \approx 0.0465\ m$$

$$t = \sqrt{s/a}\ \approx 0.043\ s$$

$$v = at\ \approx 1.075\ m/s$$

With a specific density of the milling ball of 5.9 g/cm³ (given by Fritsch, Germany), the milling ball has a kinetic energy of

$$E_{\mathrm{kin}} = 0.5\ \cdot 0.000386\ \mathrm{kg} \cdot (1.075\ \mathrm{m/s})^2 \approx 0.000223\ \mathrm{J}$$

And a force F acting upon the beaker wall of

$F = ma$ = 0.000386 kg * 24.87 m/s² ≈ 0,0096 N

Using the formula introduced by Hertz the maximum pressure can be calculated:

$$p_{\max} = \frac{1}{\pi} \sqrt[3]{\frac{1.5FE^2}{r_b^2(1-v_p^2)^2}}$$

With E being Young's modulus (= 205 GPa for stabilized ZrO_2[4]), ν_p being Poisson's ratio (0.3 for stabilized ZrO_2[4]) and r_b being the radius of the milling ball:

$p_{\max} \approx 0.156$ GPa

A milling ball just rolling at the milling beaker wall at the largest distance to the axis of the main disc:

$$F = \frac{mv^2}{r}$$

$p_{\max} \approx 0.39$ GPa

Thereby also the rotation of the beaker is taken into account.

As can be seen, the pressures calculated this way are almost one order of magnitude too small for the transition of cubic BaF_2 to orthorhombic BaF_2. This discrepancy might be explained by the fact that there will be several layers of milling balls acting upon the beaker wall. Also, there will be a distribution of impulses of the milling balls. Furthermore, the equation introduced by Hertz assumes the contact between a milling ball and a planar surface. However, the milling balls as well as the walls of the beakers will be covered with the crystallites. This can decrease the pressure acting upon the crystallites, in case of a large number of crystallites between the milling ball and the wall. In case of a small number of crystallites between milling ball and beaker wall the pressure experienced by the crystallites will be larger than calculated with the Hertz equation.

Anyway, the pressure is sufficient for the transition of the cubic BaF_2 to orthorhombic BaF_2. Hence, one might expect a complete transition of fluorite-structured BaF_2 to orthorhombic BaF_2. In fact, milling BaF_2 in tungsten carbide (WC) milling beakers with milling balls made of the same material, which is harder and much more dense than stabilized ZrO_2, results in larger amounts of orthorhombic BaF_2 than milling in ZrO_2 milling beakers with milling balls made of the same material, see fig. S11. However, milled BaF_2 consists mainly of fluorite-structure BaF_2, no matter if milled over very long times or with higher energy (higher rotation speed or heavier and harder material of the milling beaker and milling balls). Shear forces were reported to ease the reconstructive transformation process from a low-pressure to a high-pressure phase and vice versa[5-8]. Hence, the formed orthorhombic BaF_2 is probably re-transformed to fluorite-structured BaF_2, which is probably caused by low energy processes inducing shear forces at low pressures.

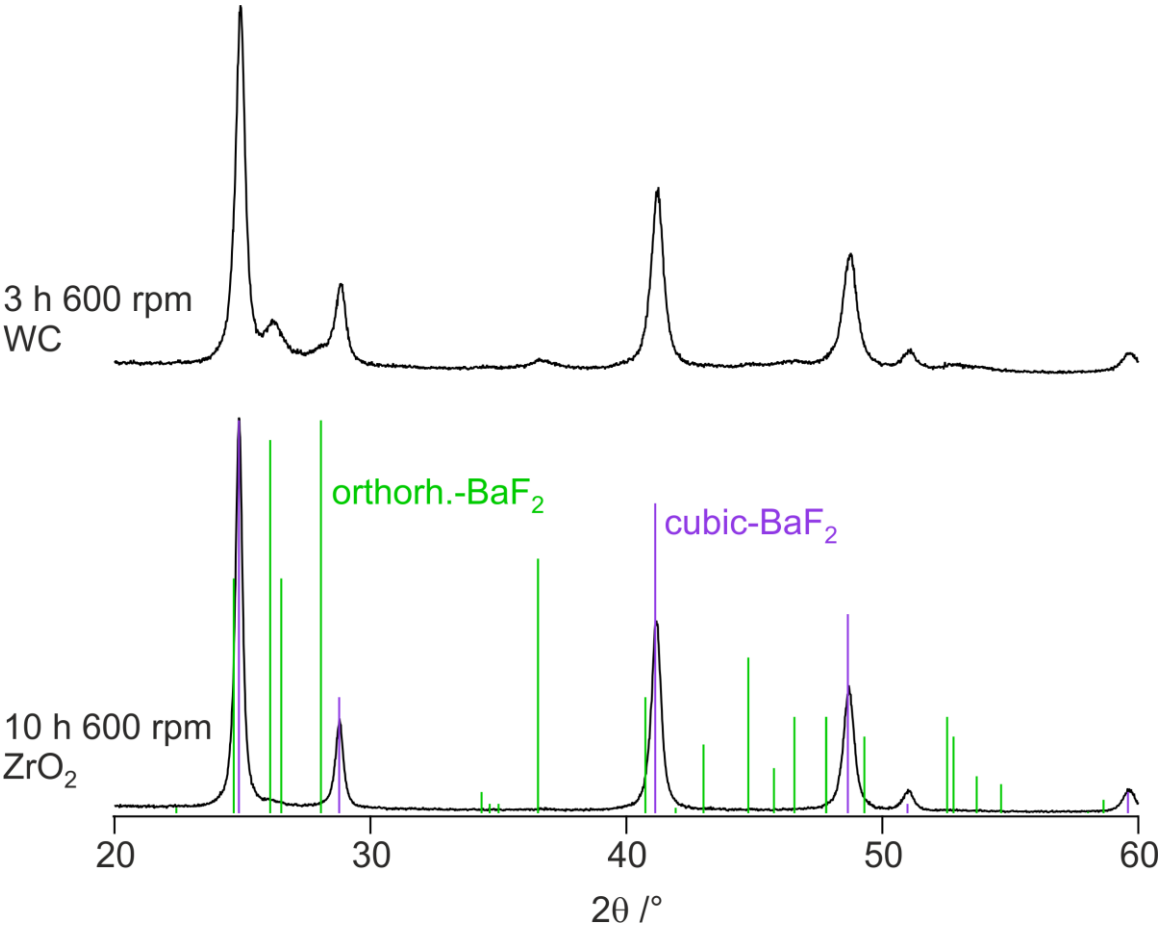

Fig. S11 XRPD patterns of milled BaF_2. One sample was milled 10 h in a milling beaker (45 mL) with milling balls (140 balls, 5 mm diameter) made of ZrO_2, the other was milled 3 h in a milling beaker (45 mL) with 100 milling balls (5 mm diameter) made of WC.

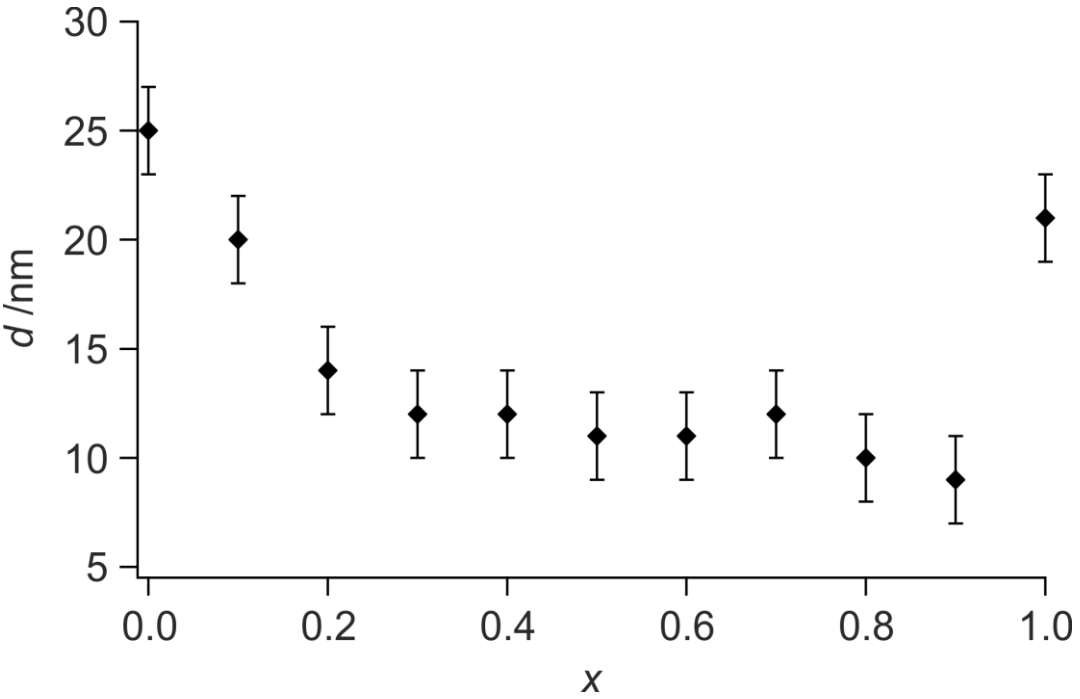

Fig. S12 Average crystallite sizes of $Ba_{1-x}Pb_xF_2$ estimated using Scherrer's equation.

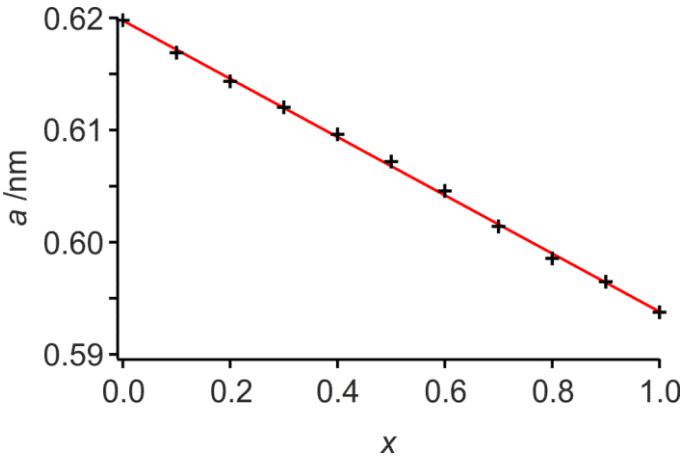

Fig. S13 Lattice parameter of fluorite-structured $Ba_{1-x}Pb_xF_2$ as a function of *x*.

In figs. S14-S16 the lattice parameters of the non-cubic $Ba_{1-x}Pb_xF_2$ as a function of *x* are shown. The fitting was done using TOPAS (Bruker) assuming cotunnite-structured material (space group *Pnma*). Deviations from a linear change are visible. This is probably caused by structural distortions of the nanocrystalline material leading to rather poor fits of the diffraction patterns. A symmetry reduction can neither be ruled out nor can it be verified due to the broad peaks. However, it should be mentioned, that in case of $Ba_{0.10}Pb_{0.90}F_2$ fitting with a monoclinic structure ($P2_1/c$) increased the quality of the fit compared to fitting the pattern assuming a cotunnite-structure.

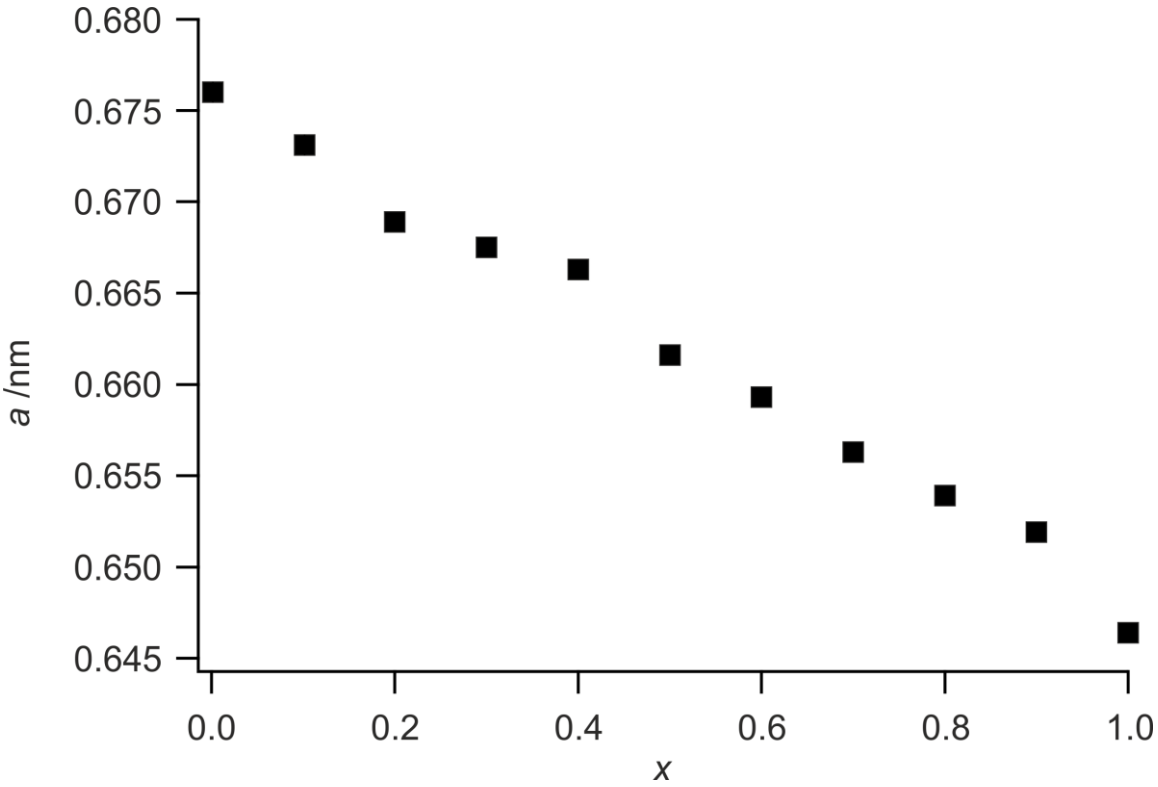

Fig. S14 Lattice parameter *a* of the orthorhombic phase of $Ba_{1-x}Pb_xF_2$.

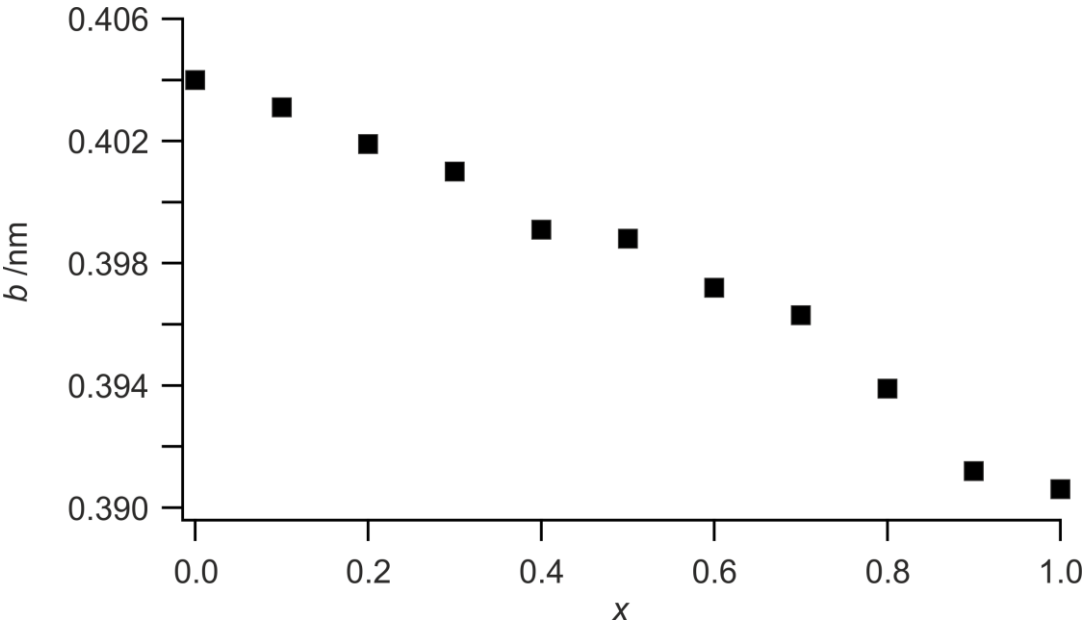

Fig. S15 Lattice parameter *b* of the orthorhombic phase of $Ba_{1-x}Pb_xF_2$.

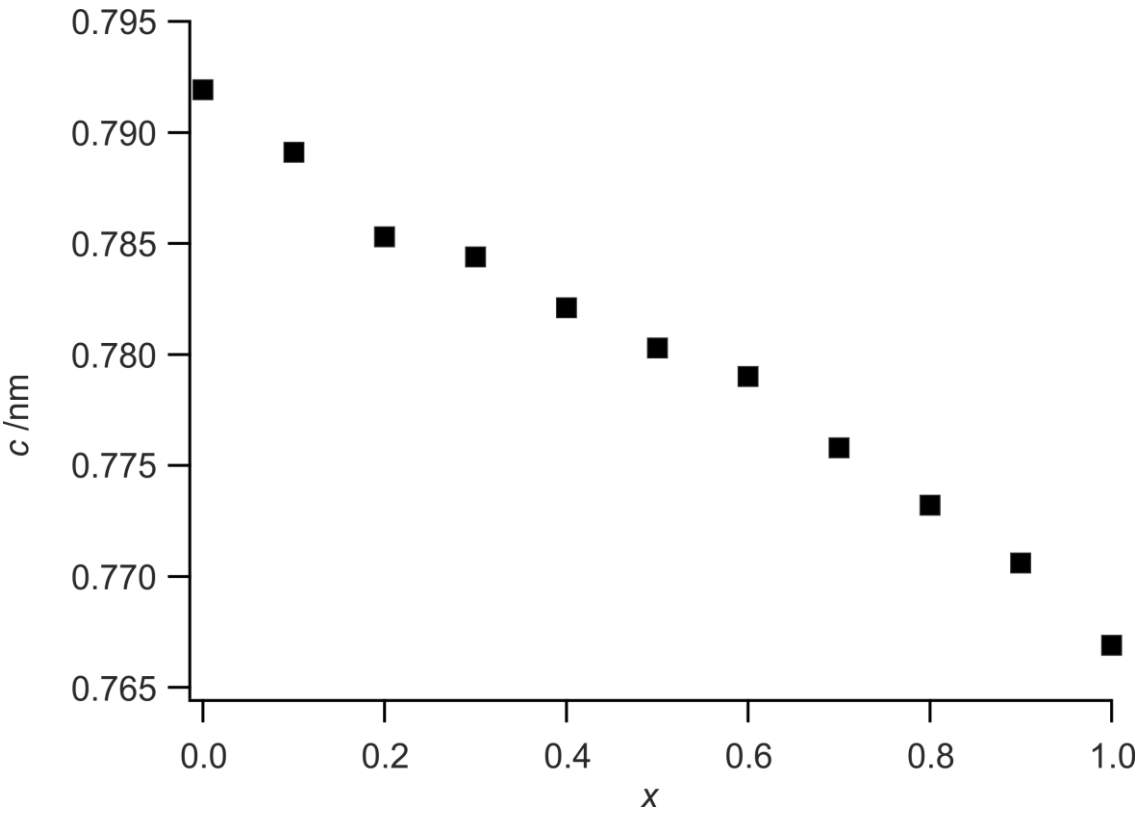

Fig. S16 Lattice parameter *c* of the orthorhombic phase of $Ba_{1-x}Pb_xF_2$.

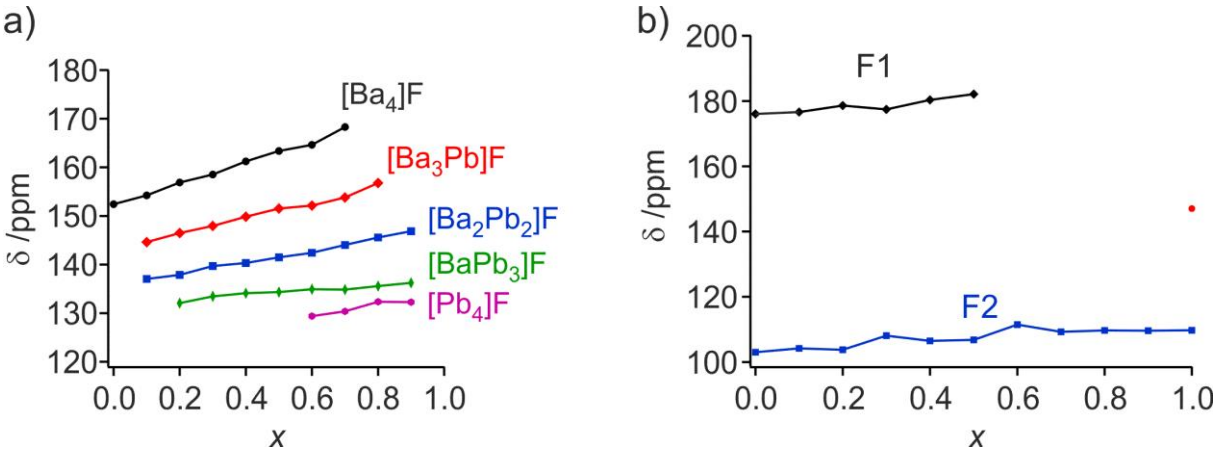

Fig. S17 a) Change of the chemical shift of the five different fluoride ion environments in fluorite-structured $Ba_{1-x}Pb_xF_2$. b) Change of the chemical shifts of the NMR lines representing fluoride ions in cotunnite-structured $Ba_{1-x}Pb_xF_2$. The red dot is the chemical shift of fluoride ions on the F1 site in α-PbF_2.

The NMR line with a chemical shift of 103 ppm in orthorhombic BaF_2, representing fluoride ions on F2 sites, shows an increase of the chemical shift value until it reaches 110 ppm of orthorhombic PbF_2 (with $Ba_{0.40}Pb_{0.60}F_2$ being an exception, showing a chemical shift of 112 ppm for unknown reasons), see fig S17b). The fluoride ions residing on F1 sites in orthorhombic BaF_2 create a signal with a chemical shift of ca. 175 ppm. With increasing Pb content the chemical shift increases up to 182 ppm, whereby the NMR line is becoming increasingly broad. Furthermore, its intensity decreases with increasing Pb

content. The increase of the chemical shift values is probably also caused by decreasing Ba-F distances due to lattice contraction caused by the introduction of smaller Pb^{2+} into the structure. Interestingly, there is no NMR line visible in the spectra for the samples with $0.50 \leq x \leq 0.90$ that can be assigned to the F1 site in orthorhombic $Ba_{1-x}Pb_xF_2$. Coming from orthorhombic PbF_2, the NMR line assigned to fluoride ions on F1 sites in orthorhombic PbF_2 at ca. 147 ppm seems to transition into the Ba_2Pb_2F environment of the fluorite structured $Ba_{1-x}Pb_xF_2$. While this could be explained by the NMR line representing fluoride ions on F1 sites being hidden by the NMR lines of the fluorite structured $Ba_{1-x}Pb_xF_2$, the vanishing of the NMR line for $x > 0.50$ coming from orthorhombic BaF_2 is unexpected due to the absence of other NMR lines in this chemical shift regime.

In fig. S18 the cubic fluorite structure and the orthorhombic cotunnite structure[9] are shown. As already mentioned, the fluoride ions are coordinated by four cations in the fluorite structure with equal cation-fluoride ion distances. In the cotunnite structure, however, the fluoride ions on F2 sites are coordinated by five cations, with three differing distances to the fluoride ion, while the fluoride ions on F1 sites are coordinated by four cations, also with three differing distances between the fluoride ion and the cations. It should be noted, that the larger chemical shift of the NMR line representing fluoride ions at the F1 site is due to a smaller distance between Pb^{2+} and F^- compared to the situation at the F2 site[1].

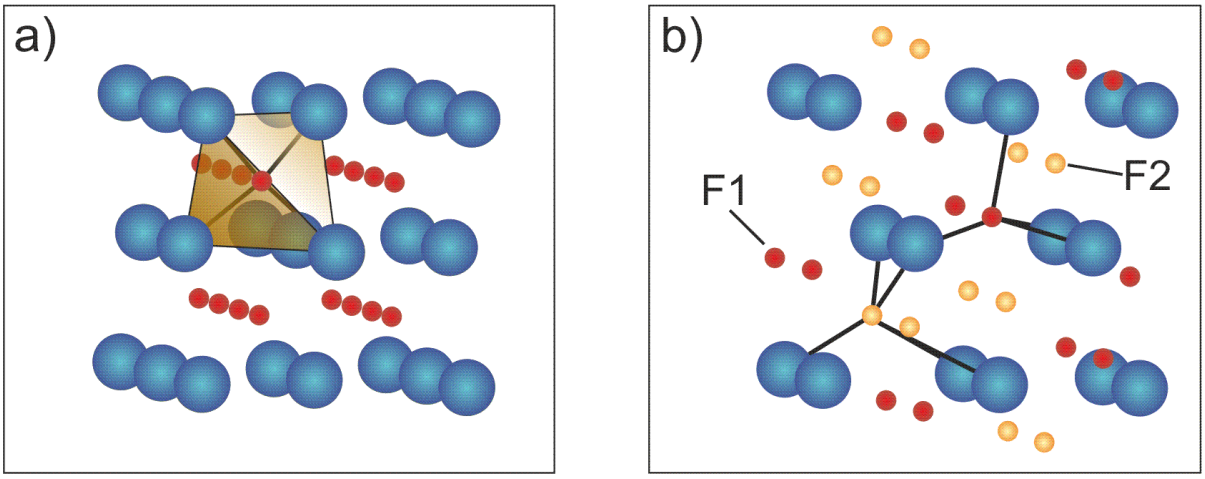

Fig. S18 a) cubic fluorite structure, with cations colored blue and anions colored red. b) orthorhombic cotunnite structure with cations colored blue, anions on F1 sites colored red and anions on F2 sites colored orange.

If we now substitute cations in the fluorite structure with a cation species of clearly different size, we can expect structural disorder on the local scale. Thus, the distances between the four cations and the fluoride ion will most likely not be equal anymore[2], as was already discussed for $Sr_{1-x}Pb_xF_2$. That way the cationic environment of the fluoride ion will become more similar to the one of the fluoride ions on F1 sites. Thus, it seems possible, that the decrease of the intensity of the F1 NMR line, coming from orthorhombic BaF_2, and the apparent transition of the F1 NMR line coming from orthorhombic PbF_2 into the Pb_2Ba_2 environment of the fluorite-structured $Ba_{1-x}Pb_xF_2$ might be explained by the F1 environment also becoming more and more similar to the fluoride environment in the disordered cubic fluorite structure due to the cation substitution. Thus, coming from orthorhombic BaF_2, the F1 NMR line would represent the fluoride ions at F1 sites, which

are yet only indirectly affected by the cation substitution, i.e. experience only a slight decrease of $d(M\text{-F})$ due to neighboring environments containing Pb^{2+}, while the fluoride ions on F1 sites coordinated by different cation species are represented by ^{19}F NMR lines similar to the ones of the fluoride ions in cation mixed environments in the fluorite-structured $Ba_{1-x}Pb_xF_2$.

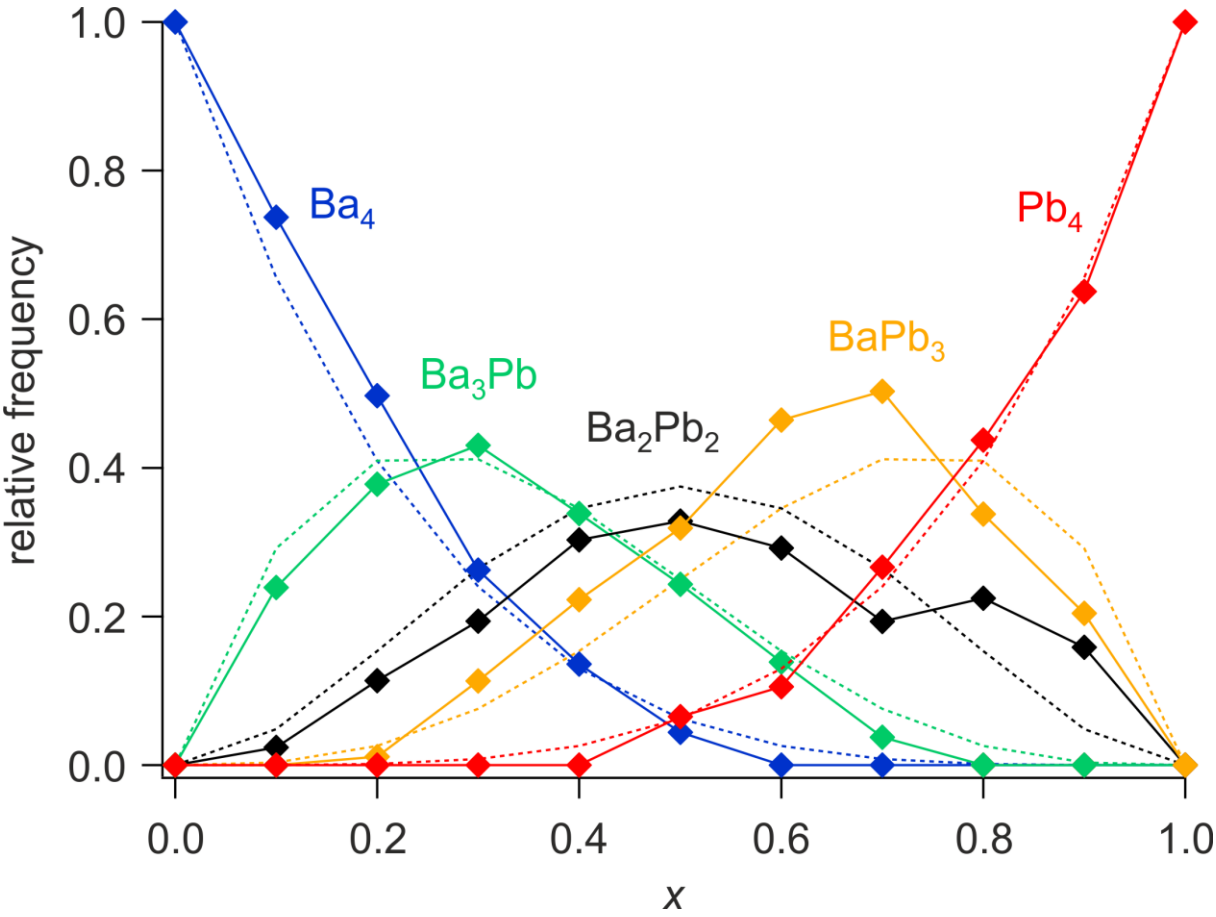

Fig. S19 Relative frequencies of the five cation environments of fluoride ions in $Ba_{1-x}Pb_xF_2$. The dotted lines show the relative frequencies of the environments in case of a random distribution of the two cation species.

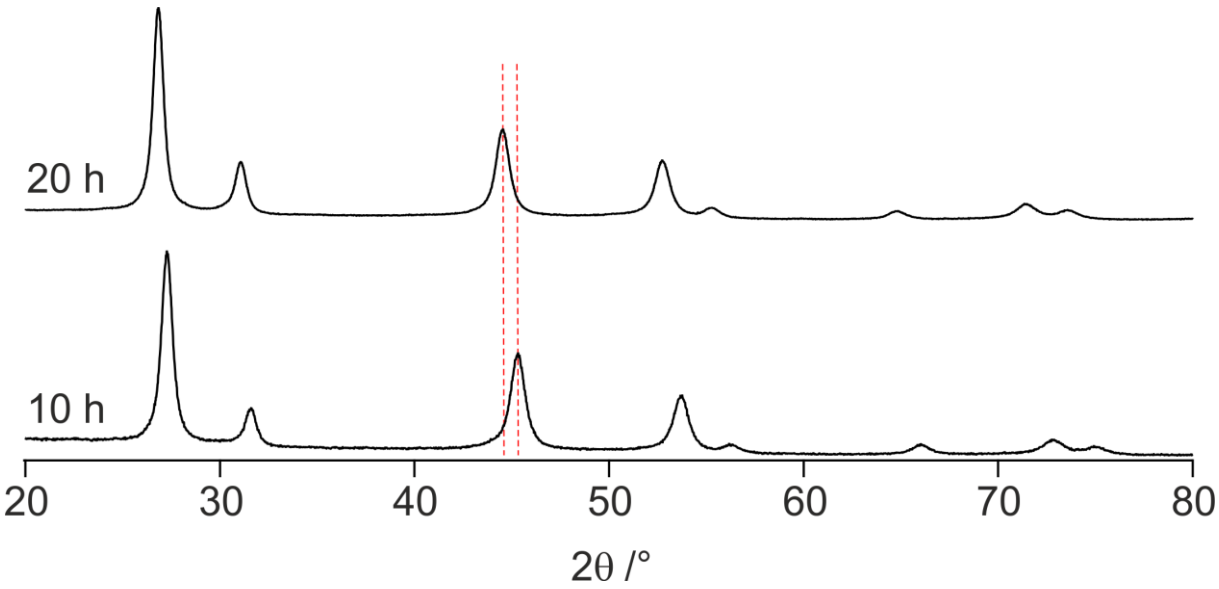

Fig. S20 XRPD patterns of mixtures to give $Ca_{0.40}Pb_{0.60}F_2$ milled for the times indicated.

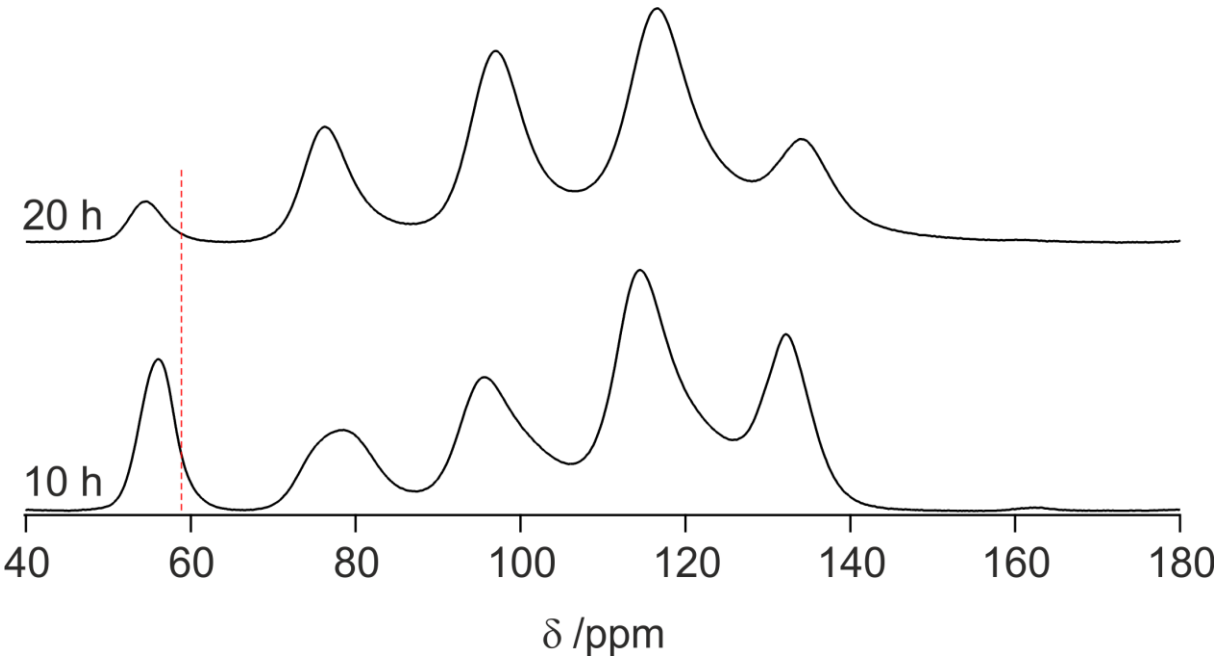

Fig. S21 ^{19}F MAS NMR spectra (ν_0 = 564.7 MHz, ν_{rot} = 60 kHz) of mixtures to give $Ca_{0.40}Pb_{0.60}F_2$ milled for the times indicated. The dotted line indicates the chemical shift of pure CaF_2.

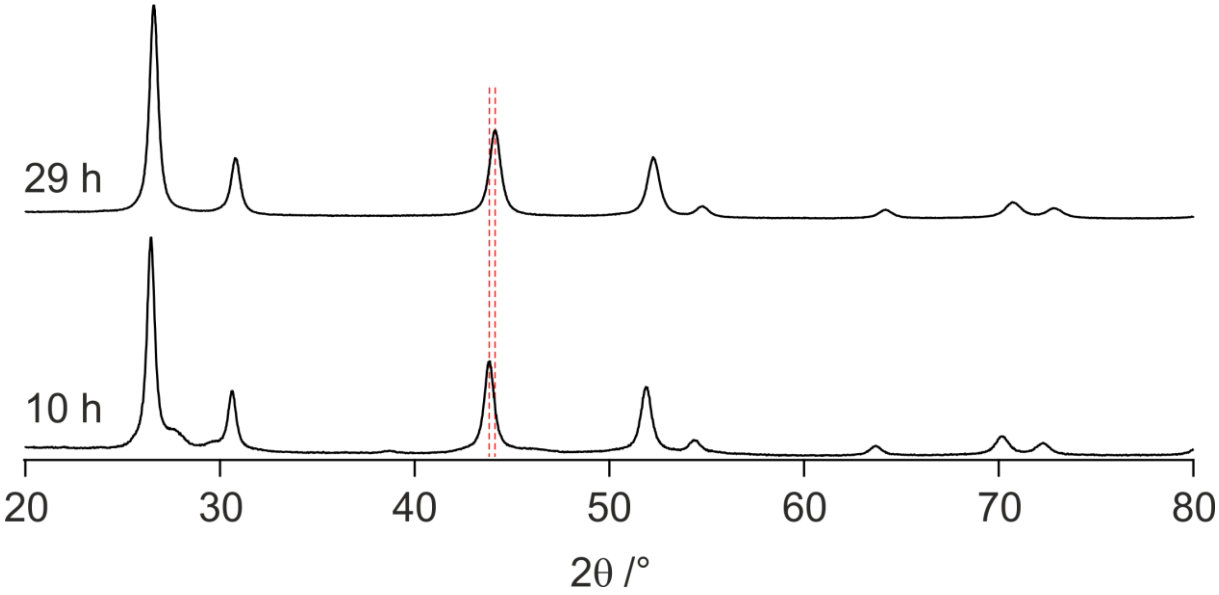

Fig. S22 XRPD patterns of mixtures to give $Ca_{0.30}Pb_{0.70}F_2$ milled for the times indicated.

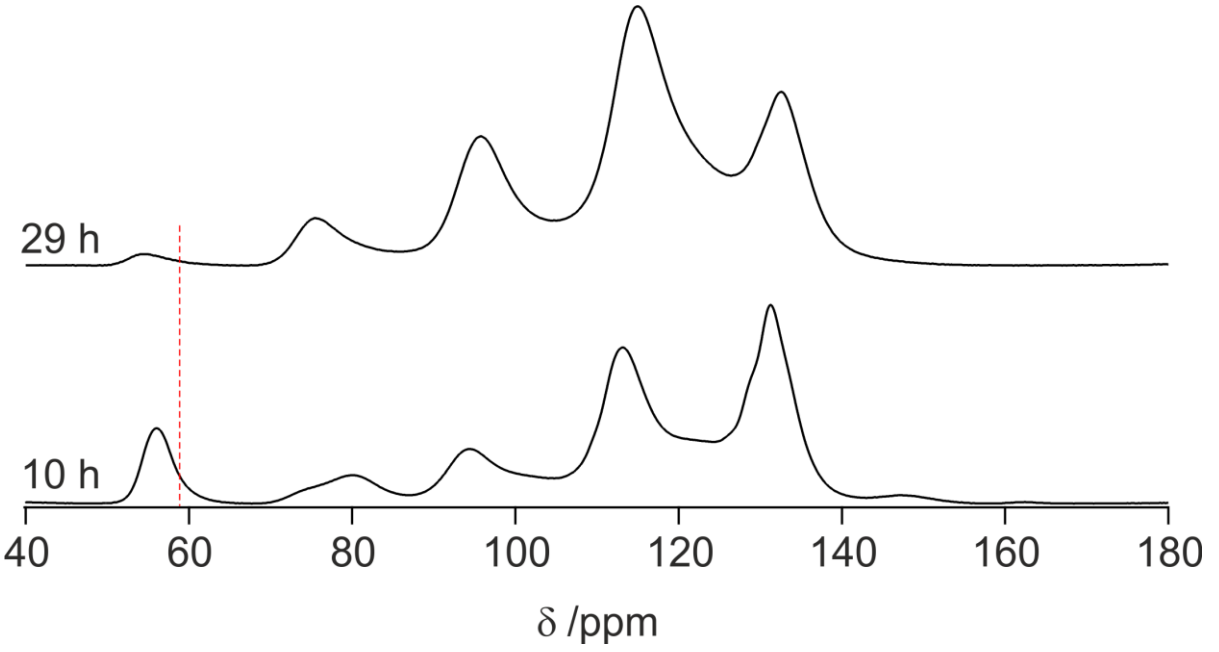

Fig. S23 ^{19}F MAS NMR spectra (ν_0 = 564.7 MHz, ν_{rot} = 60 kHz) of mixtures to give $Ca_{0.30}Pb_{0.70}F_2$ milled for the times indicated. The dotted line indicates the chemical shift of pure CaF_2.

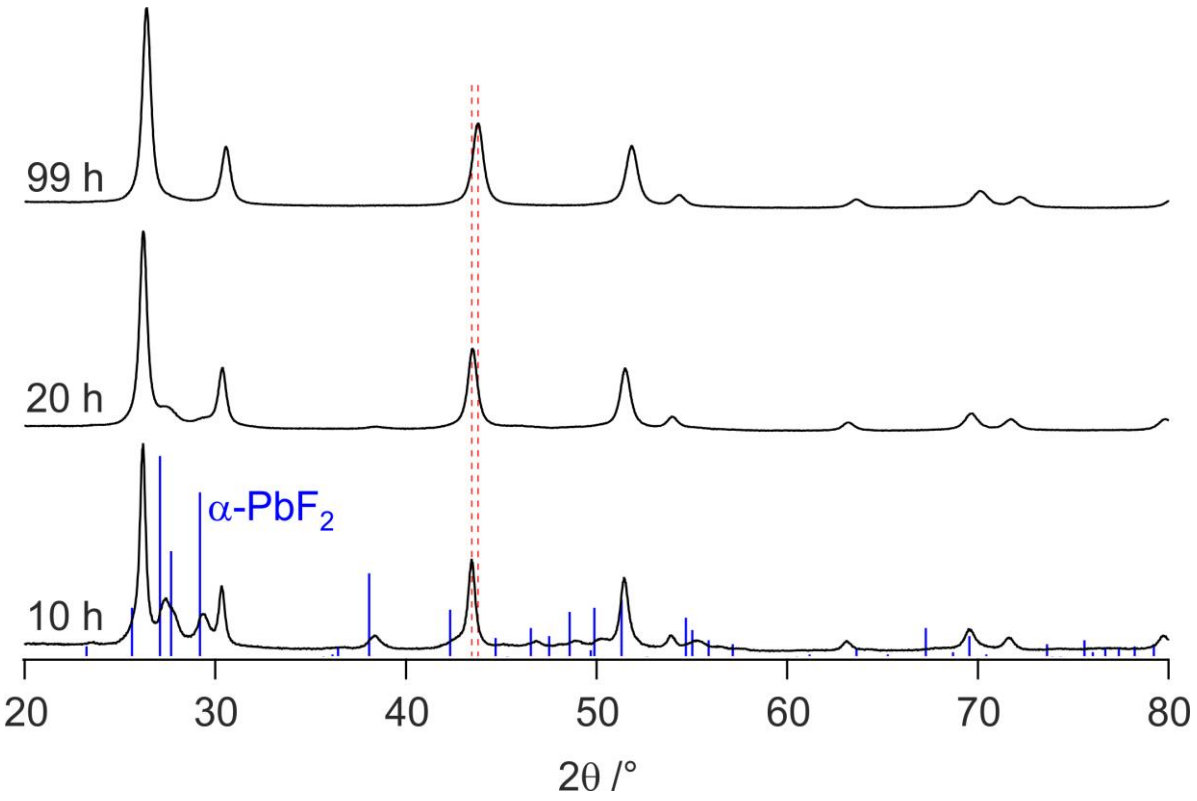

Fig. S24 XRPD patterns of mixtures to give $Ca_{0.20}Pb_{0.80}F_2$ milled for the times indicated.

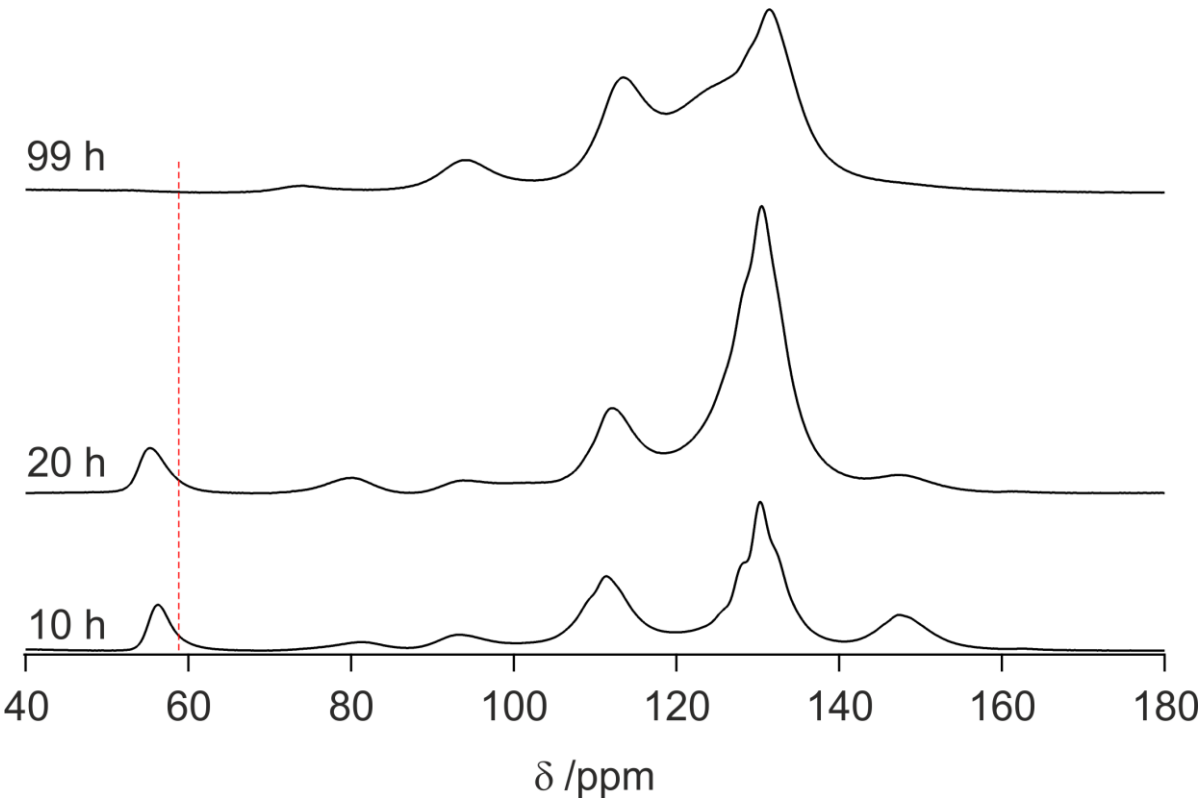

Fig. S25 ^{19}F MAS NMR spectra (ν_0 = 564.7 MHz, ν_{rot} = 60 kHz) of mixtures to give $Ca_{0.20}Pb_{0.80}F_2$ milled for the times indicated. The dotted line indicates the chemical shift of pure CaF_2.

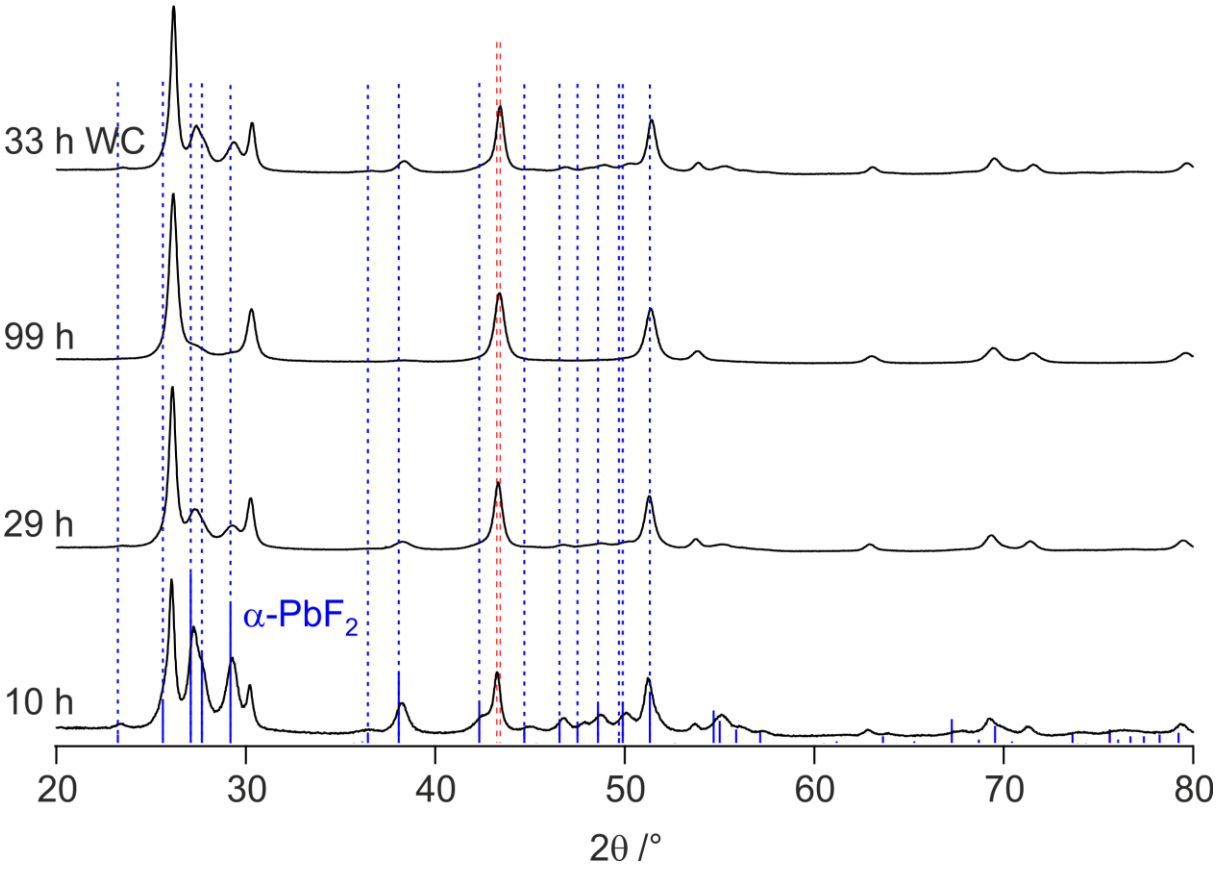

Fig. S26 XRPD patterns of mixtures to give $Ca_{0.10}Pb_{0.90}F_2$ milled for the times and under the conditions indicated in the figure.

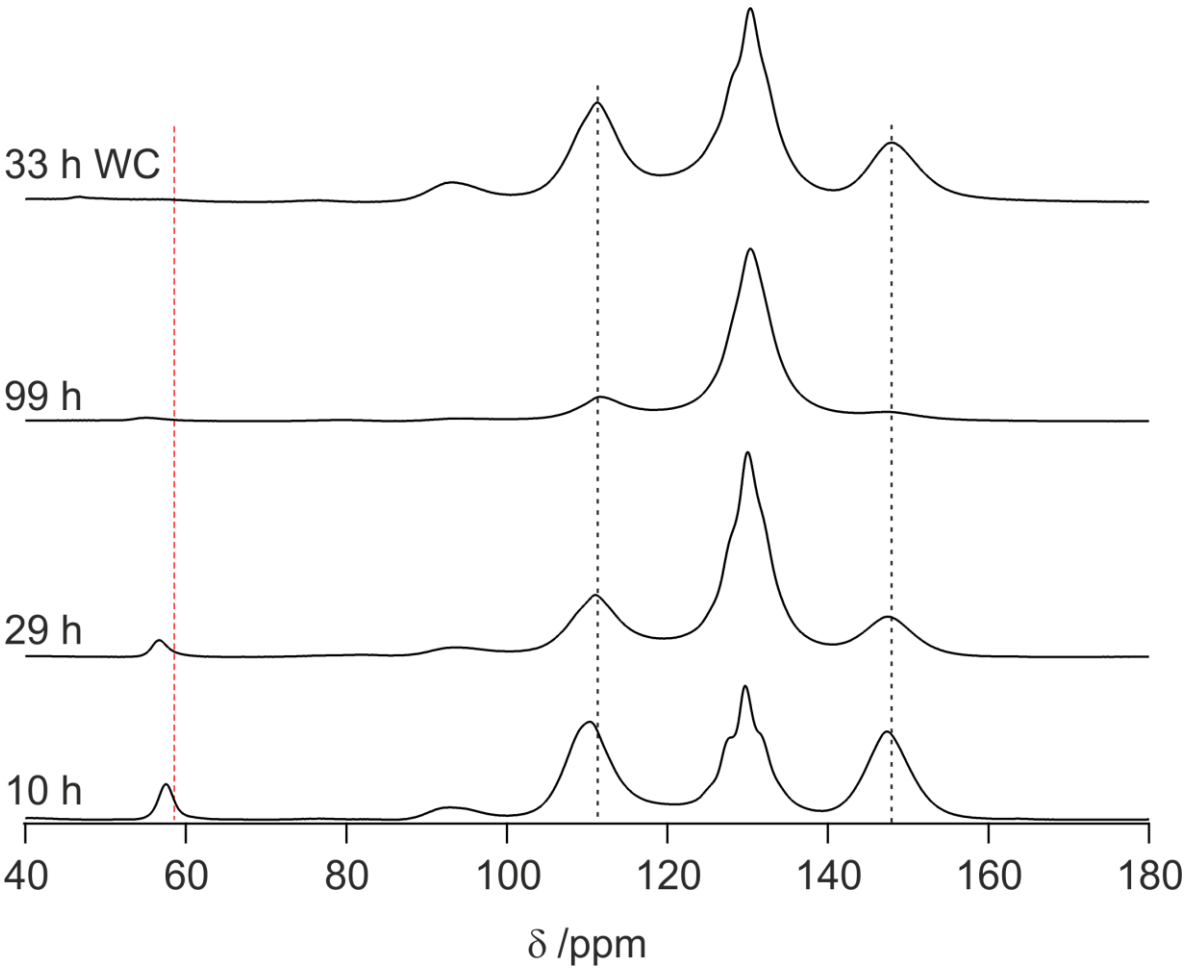

Fig. S27 ^{19}F MAS NMR spectra (ν_0 = 564.7 MHz, ν_{rot} = 60 kHz) of mixtures to give $Ca_{0.10}Pb_{0.90}F_2$ milled for the times and under the conditions indicated in the figure. The red dotted line indicates the chemical shift of pure CaF_2.

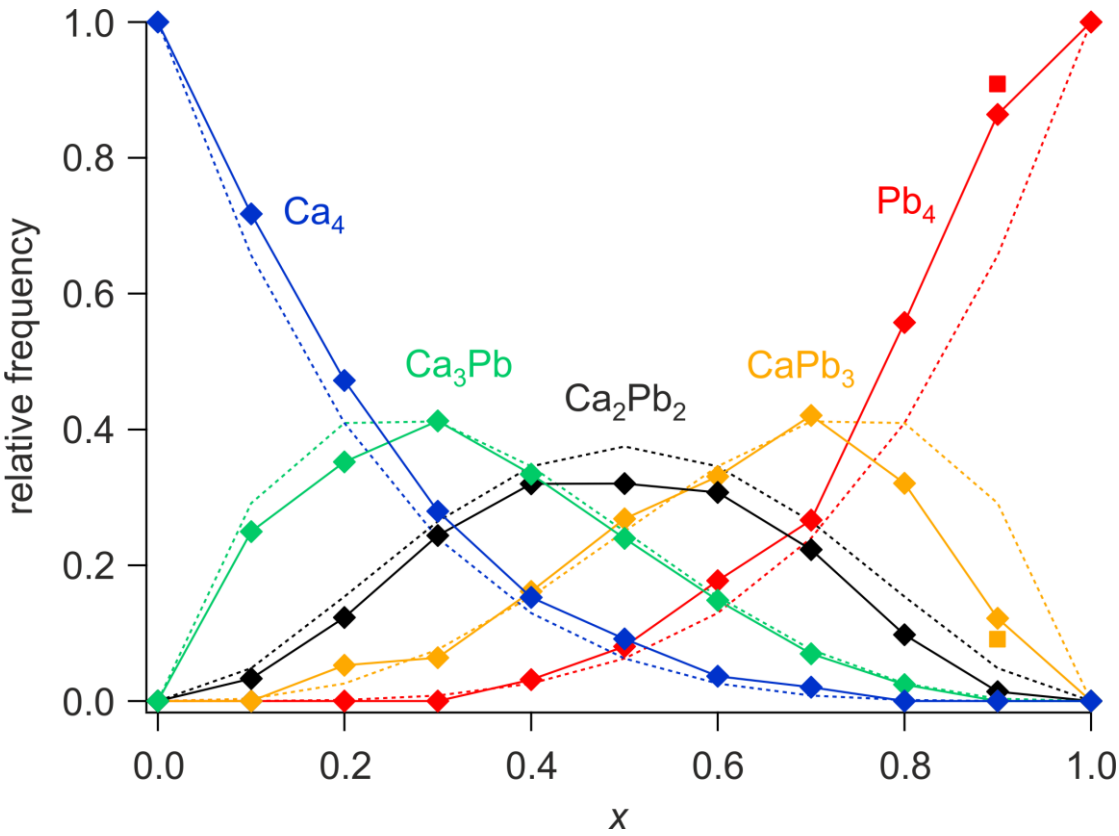

Fig. S28 Relative frequencies of the five cation environments of fluoride ions in $Ca_{1-x}Pb_xF_2$. The dotted lines show the relative frequencies of the environments in case of a random distribution of the two cation species. Calculations were done in case of $x > 0.50$ for the long-milled samples (20 h, 29 h and 99 h). The rectangles show the values of annealed $Ca_{0.10}Pb_{0.90}F_2$ (see Fig S34).

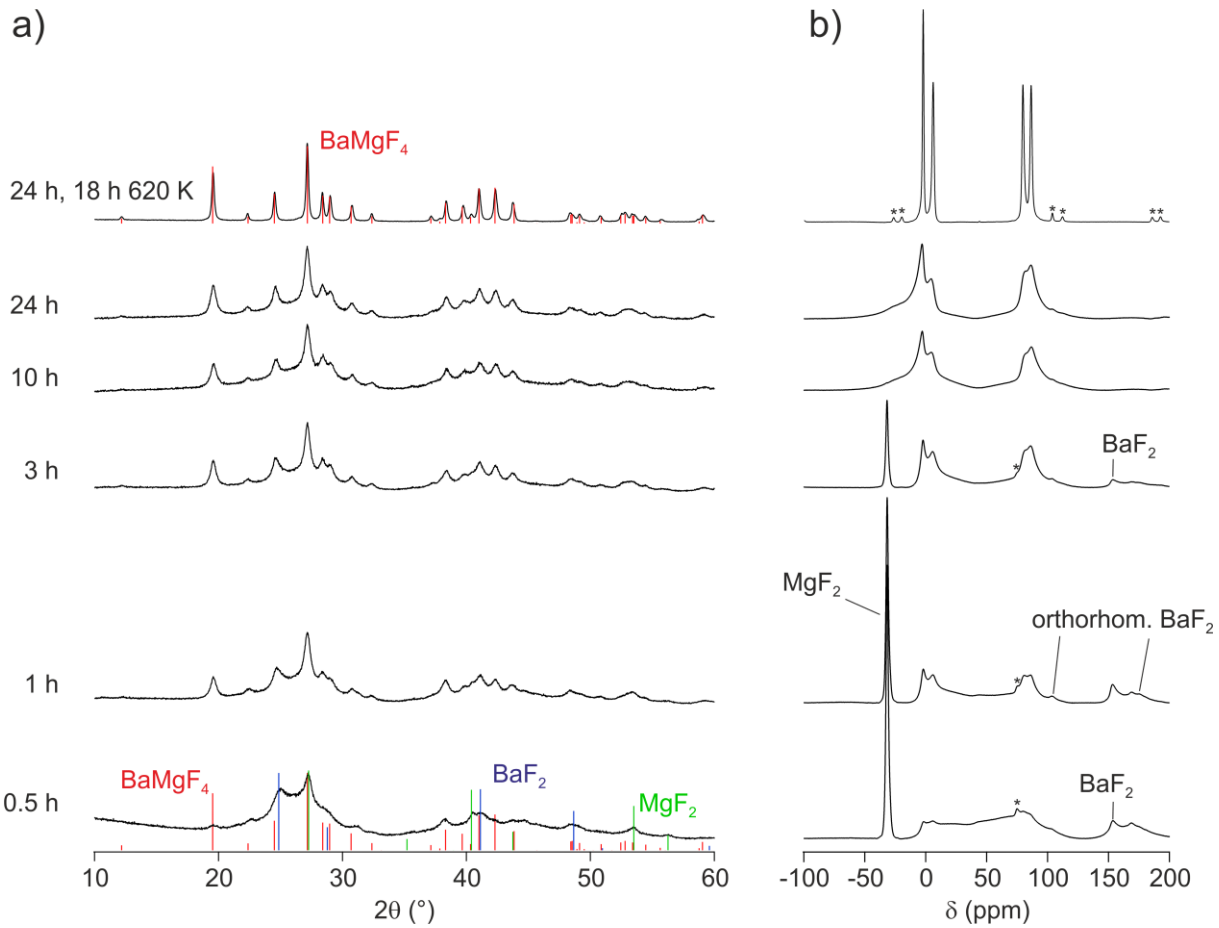

Fig. S29 a) XRPD patterns of equimolar mixtures of BaF_2 and MgF_2 milled at 600 rpm in milling beakers (45 mL) made of stabilized ZrO_2 with 140 milling balls (diameter = 5 mm) in a Fritsch Pulverisette 7 premium line planetary ball mill for the durations indicated in the figure. b) corresponding ^{19}F MAS NMR spectra. Spinning side bands are marked with asterisks. After 24 h of milling the formation of $BaMgF_4$ seems to be completed.

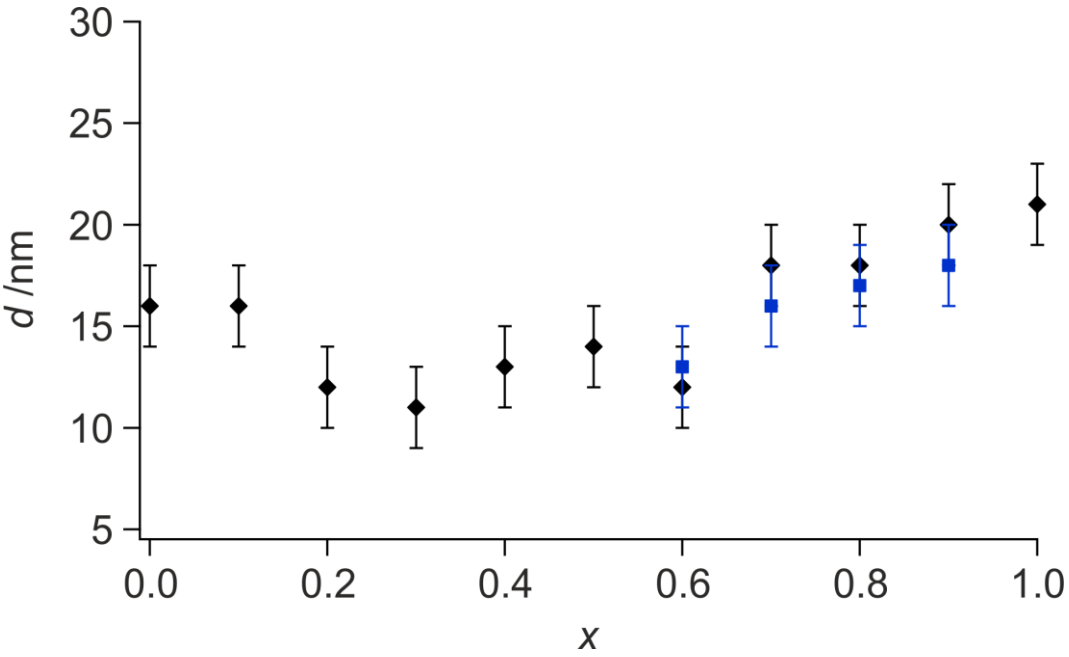

Fig. S30 Average crystallite sizes of $Ca_{1-x}Pb_xF_2$ estimated using Scherrer's equation. The blue symbols show the average crystallite sizes of the samples milled for 20 h (x = 0.60), 29 h (x = 0.70) or 99 h (x = 0.80 and x = 0.90).

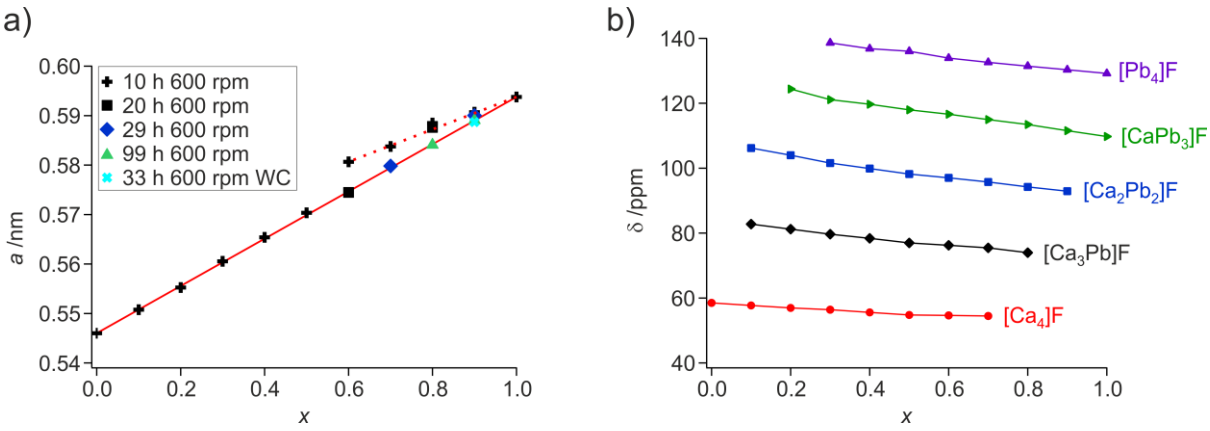

Fig. S31 Left: Lattice parameter of cubic fluorite-structured $Ca_{1-x}Pb_xF_2$ solid solutions as a function of x. The dotted line shows the change of the lattice parameter for the mixtures milled for only 10 h for x > 0.50. Right: Chemical shifts of the different NMR lines visible in the ^{19}F MAS NMR spectra of $Ca_{1-x}Pb_xF_2$ as a function of x.

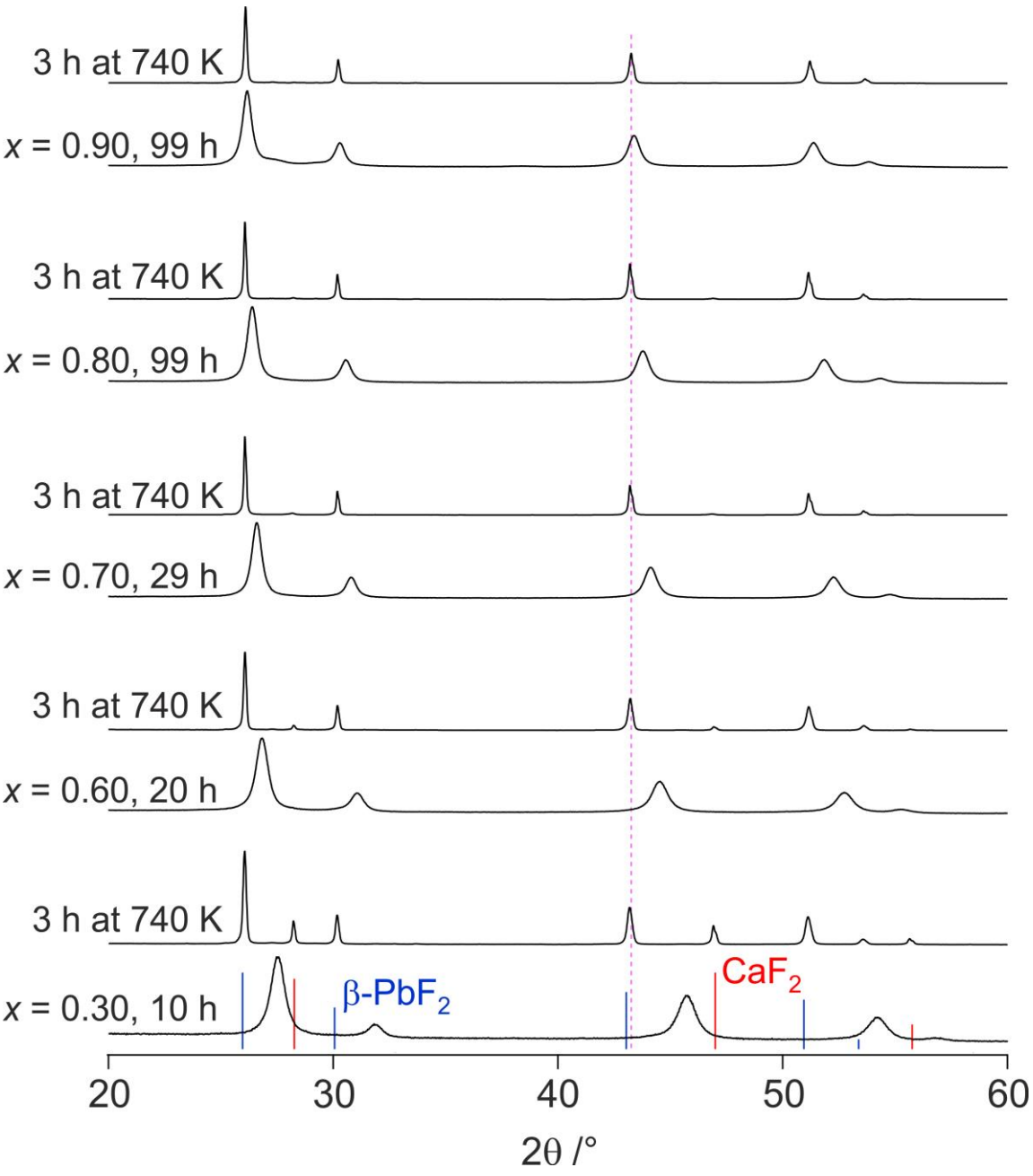

Fig. S32 XRPD patterns of some of the $Ca_{1-x}Pb_xF_2$ samples before and after annealing.

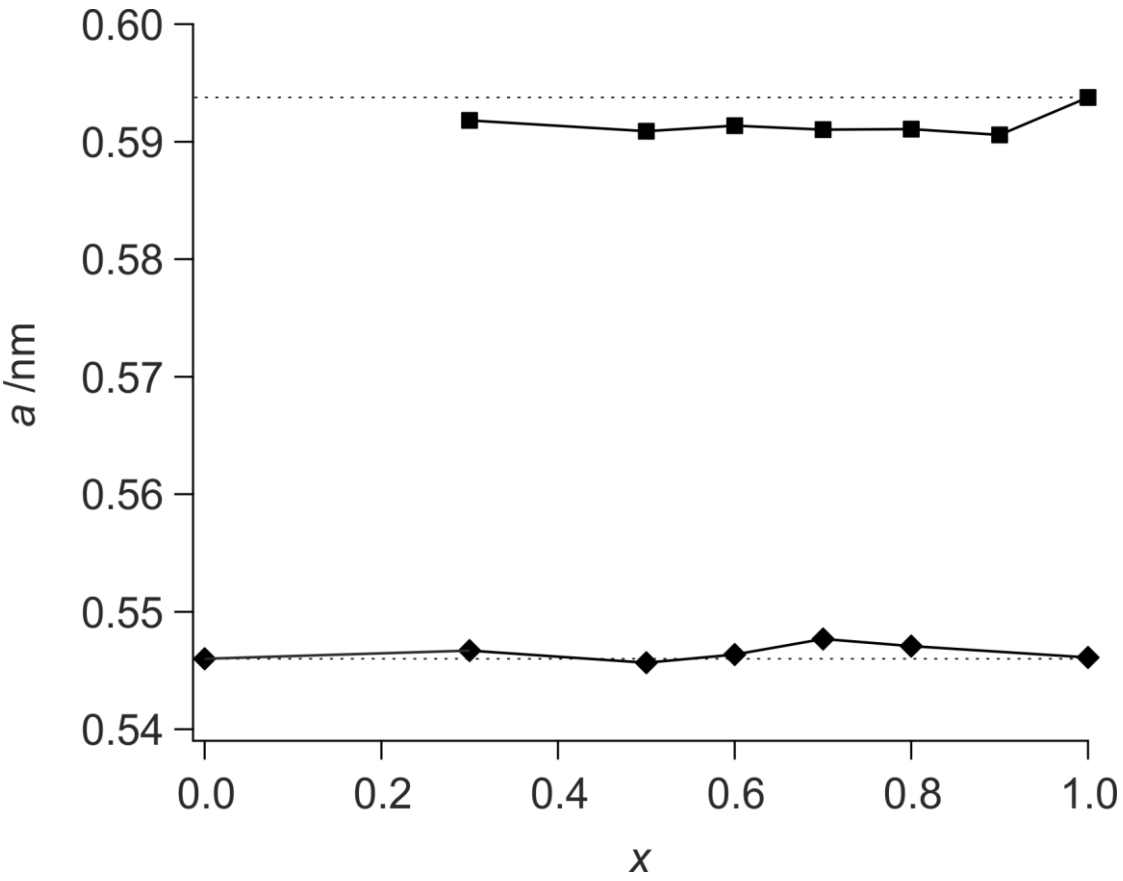

Fig. S33 Lattice parameters of several $Ca_{1-x}Pb_xF_2$ samples after annealing for 3 h at 740 K under Ar. The dotted lines indicate the lattice parameters of pure β-PbF_2 and CaF_2. The lines are meant to guide the eye.

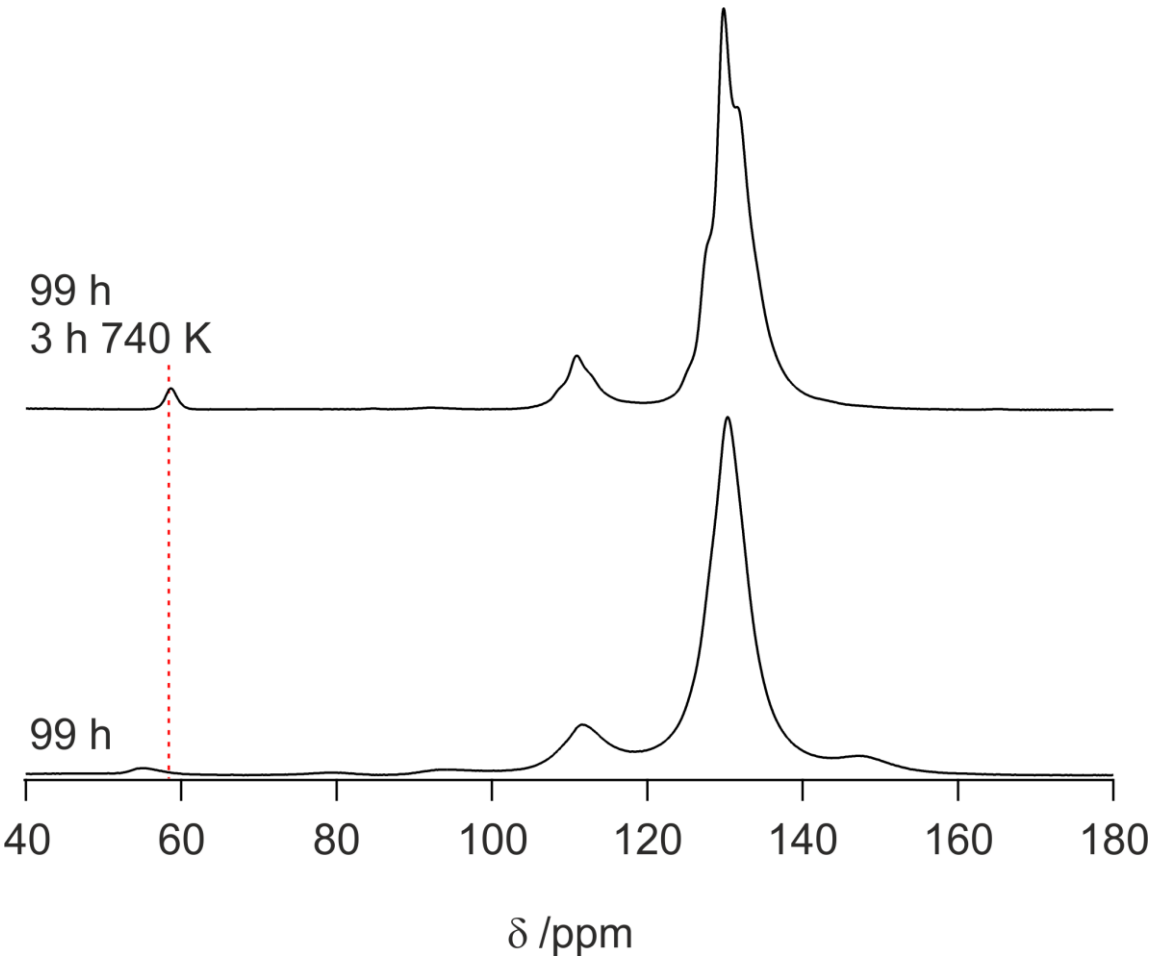

Fig. S34 ^{19}F MAS NMR spectra (ν_0 = 564.7 MHz, ν_{rot} = 60 kHz) of $Ca_{0.10}Pb_{0.90}F_2$ before and after annealing. The dotted line shows the chemical shift of CaF_2.

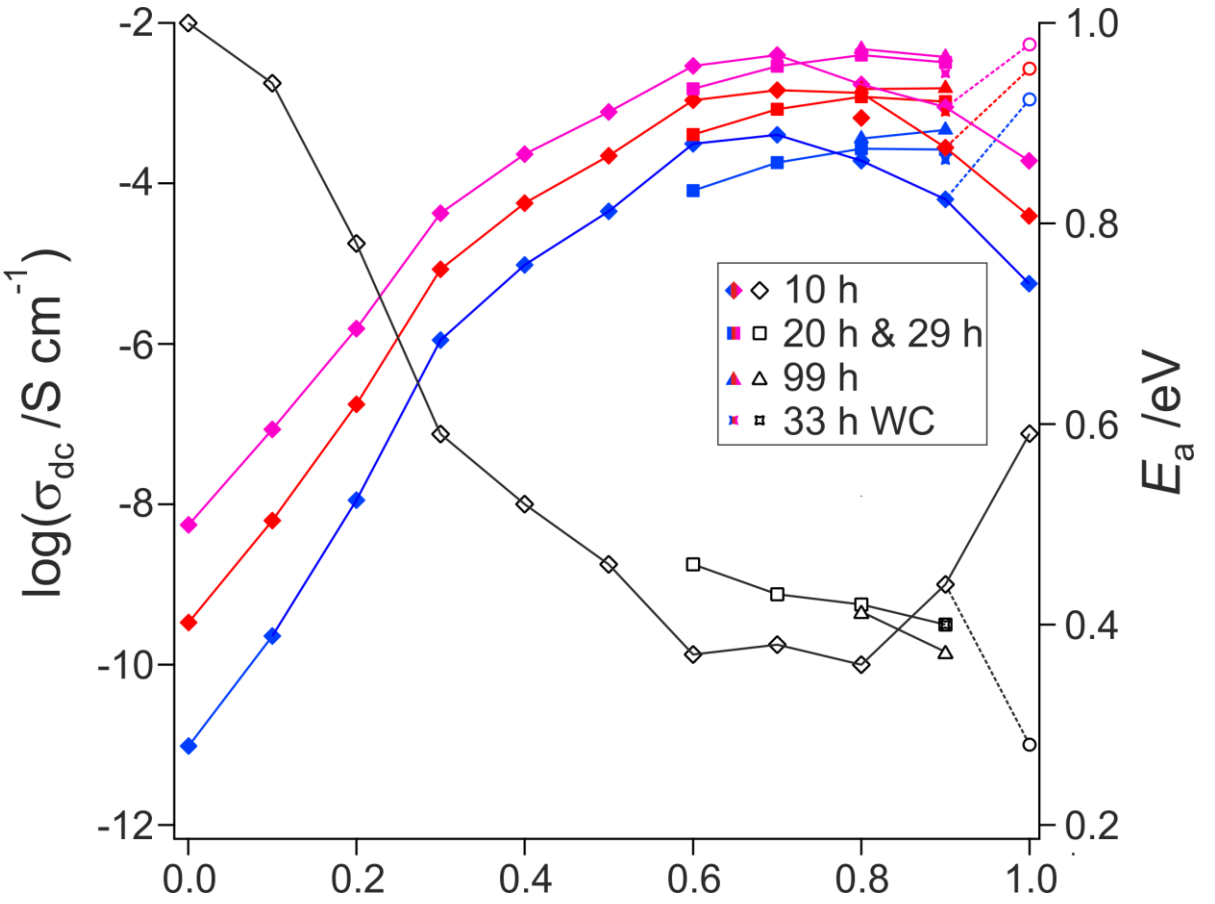

Fig. S35 Dc conductivities and activation energies of all $Ca_{1-x}Pb_xF_2$ samples as a function of *x* for three different temperatures.

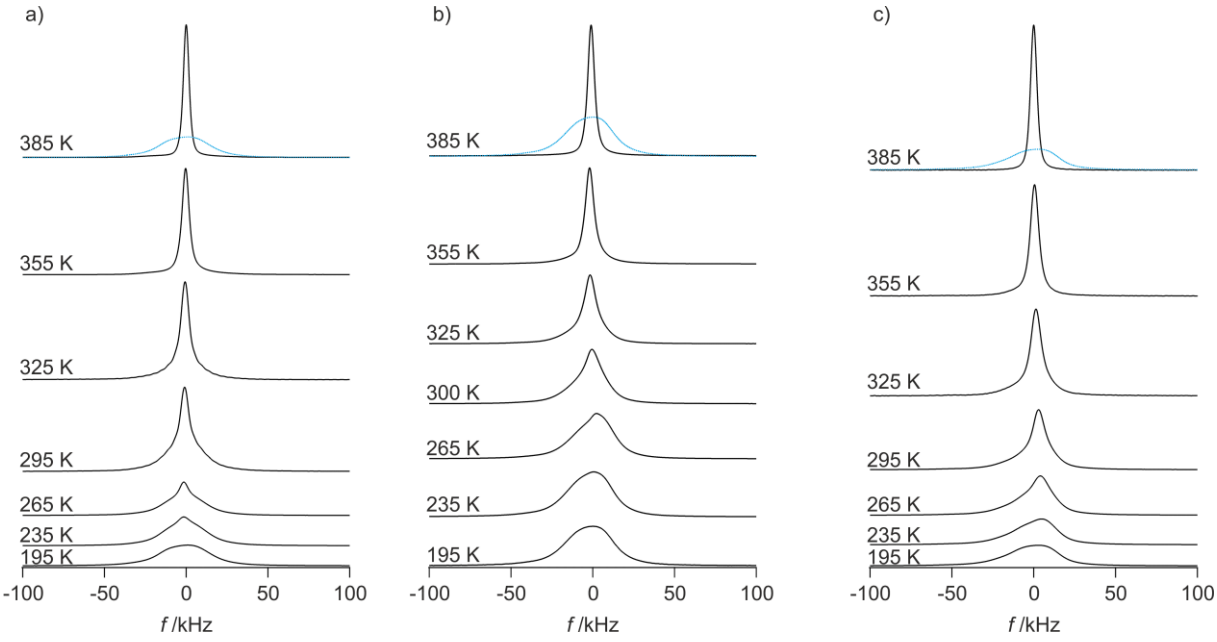

Fig. S36 Static ^{19}F NMR spectra (ν_0 = 564.7 MHz) of a) $Ba_{0.10}Pb_{0.90}F_2$, b) $Sr_{0.10}Pb_{0.90}F_2$ and c) $Ca_{0.10}Pb_{0.90}F_2$. The spectra recorded at the lowest temperature (dotted blue line) and the ones recorded at the highest temperature are superimposed for comparison.

References

(1) B. Bureau, G. Silly, J.Y. Buzaré, Superposition Model for ^{19}F Isotropic Chemical Shift in Ionic Fluorides: From Basic Metal Fluorides to Transition Metal Fluoride Glasses. Chem. Phys., 1999, 249, 89-104.

(2) A. Düvel, P. Heitjans, P.P. Fedorov, G. Scholz, G. Cibin, A.V. Chadwick, D.M. Pickup, S. Ramos, L.W.L. Sayle, E.K. Sayle, T.X.T. Sayle, D.C. Sayle, Is Geometric Frustration-Induced Disorder a Recipe for High Ionic Conductivity? J. Am. Chem. Soc., 2017, 139, 5842-5848.

(3) X. Mu, W. Sigle, A. Bach, D. Fischer, M. Jansen, P.A. van Aken, Influence of a Second Cation (M = Ca^{2+}, Mg^{2+}) on the Phase Evolution of $(Ba_xM_{1-x})F_2$ Starting from Amorphous Deposits. Z. Anorg. Allg. Chem., 2014, 640, 1868-1875.

(4) W. Papst, G. Tichá, E. Gregorová, Effective Elastic Properties of Alumina-Zirconia Composite Ceramics – Part 3. Calculation of Elastic Moduli of Polycrystalline Alumina and Zirconia from Monocrystal Data. Ceramics Silikáty, 2004, 48, 41.

(5) S.M. Dorfman, F. Jiang, Z. Mao, A. Kubo, Y. Meng, V.B. Prakapenka, T.S. Duffy, Phase Transition and Equations of State of Alkali Earth Fluorides CaF_2, SrF_2 and BaF_2 to Mbar Pressures. Phys. Rev. B, 2010, 81, 174121.

(6) J.S. Smith, S. Desgreniers, J.S. Tse, J. Sun, D.D. Klug, Y. Ohishi, High-Pressure Structured and Vibrational Spectra of Barium Fluoride: Results Obtained Under Nearly Hydrostatic Conditions. Phys. Rev. B, 2009, 79, 134104.

(7) F. Dachille, R. Roy, High-Pressure Phase Transformations in Laboratory Mechanical Mixers and Mortars. Nature, 1960, 186, 34-71.

(8) R.Roy, Accelerating the Kinetics of Low-Temperature Inorganic Syntheses. J. Solid State Chem., 1994, 111, 11-17.

(9) J.M. Leger, J. Haines, A. Atouf, O. Schulte, S. Hull, High-Pressure X-Ray- and Neutron Diffraction Studies of BaF_2: An Example of a Coordination Number of 11 in AX_2 Compounds. Phys. Rev. B, 1995, 52, 13247-13256.